Full Title (171/250 characters): Selective neurodevelopmental and behavioral deficits in *Scrib* conditional knock-out mice recapitulate some phenotypes associated with the Verheij/8q23.4 deletion syndrome.

Jerome Ezan[1,2], Maité M. Moreau[1,2], Tamrat M. Mamo[1,2], Miki Shimbo[1,2], Maureen Decroo[1,2], Melanie Richter[3], Ronan Peyroutou[1,2], Rivka Rachel[4], Fadel Tissir[5] , Froylan Calderon de Anda[3], Nathalie Sans[1,2] and Mireille Montcouquiol[1,2]

1. INSERM U1215, Neurocentre Magendie, Bordeaux, France.

2. University of Bordeaux, Bordeaux, France.

3. Germany Center for Molecular Neurobiology Hamburg (ZMNH), Research Group Neuronal Development, University Medical Center Hamburg-Eppendorf, Hamburg, Germany.

4. Neurobiology-Neurodegeneration and Repair Laboratory, National Eye Institute, NIH, Bethesda, Maryland 20892, USA.

5. University of Louvain, Institute of Neuroscience, Developmental Neurobiology Group, Avenue Mounier 73, Box B1.73.16, 1200 Brussels, Belgium.

Corresponding authors: Dr. Mireille Montcouquiol and Dr. Jerome Ezan, INSERM-U1215, Neurocentre Magendie

E-mail: mireille.montcouquiol@inserm.fr Tel: +33 5 5757 3762. Fax: +33 5 5757 3752

jerome.ezan@inserm.fr Tel: +33 5 5757 3749. Fax: +33 5 5757 3752

Competing financial interests: The authors declare no competing financial interests.

Manuscript information: 6 figures, 6 supplementary figures

Short Title (105/105 characters): Genetic dissection of *Scrib* functions during forebrain development and its relevance to Verheij syndrome.

Abstract (226/300 words)

Neurodevelopmental disorders often arise from combined defects in processes including cell proliferation, differentiation, neuronal migration, axonal pathfinding and commissure formation. Cell polarity proteins serve as a nexus to transduce signals for the establishment of these essential processes. Scribble (Scrib) is an evolutionarily conserved polarity protein that is known to regulate the establishment of apicobasal and planar cell polarity. Mutations in the human *SCRIB* gene are associated with neural tube defects and this gene is located in the minimal critical region deleted in the rare Verheij/8q24.3 deletion syndrome. In the present study, we evaluated the contribution of Scrib to some of the neurological features found in patients with this syndrome, including microcephaly and corpus callosum agenesis. Using various brain-specific conditional mouse mutants and *in utero* electroporation experiments, we assessed the impact of the spatio-temporal selective *Scrib* deletion on brain morphogenesis and animal behavior. Our results showed that global embryonic deletion of *Scrib* in the telencephalon lead to a reduction of cortical thickness and an alteration of interhemispheric connectivity. In addition, we identified cell-autonomous effects of Scrib on neuronal migration, and we suggest a non-cell-autonomous effect in axonal guidance. Finally, comparative behavioral analysis showed that mice with *Scrib* invalidation have psychomotor deficits. Altogether, our mouse models recapitulate a number of the phenotypes associated with Verheij/8q24.3 deletion syndrome patients, supporting the possibility that *Scrib* contributes to this rare disease.

Key words: Scrib ; Verheij/8q24.3 deletion syndrome ; contiguous gene syndrome ; planar cell polarity PCP; neurodevelopmental disorders ; microcephaly ; corpus callosum

Author Summary (176/200 words)

The mammalian brain, seat of cognitive and behavioral processing, is the result of numerous, complex but coordinated mechanisms of development such as cell proliferation, migration, neuritogenesis, synaptogenesis and neural network formation. Patients with disruptions in these fundamental processes will typically exhibit neurodevelopmental disorders. As such, the rare Verheij syndrome is a condition where patients display some neurological features such as microcephaly (dramatic reduction in brain cortical size) or agenesis of the corpus callosum (loss of the main commissure between hemispheres). The human gene *SCRIB* is included within a region, identified as 8q24.3, which is deleted in patients with this syndrome. In this paper, we generated mouse models to assess the consequences of selective genetic inactivation of Scrib on the brain architecture and function. From the neuroanatomical standpoint, we show that Scrib controls the formation of the cerebral cortex and the corpus callosum. This is correlated with behavioral deficits such as disrupted locomotion, learning and memory. Altogether, this work validates the association between *Scrib* loss and the brain-associated clinical features observed in individuals with Verheij/8q24.3 deletion syndrome.

Introduction

Verheij syndrome, also called 8q24.3 deletion syndrome (VRJS, OMIM #615583), is characterized by complex features such as growth retardation, short stature, dysmorphic facial features as well as renal and cardiac defects [1,2]. The neurological symptoms of this syndrome include delayed psychomotor development, mild intellectual disability and epilepsy that are frequently associated with neurodevelopmental defects such as microcephaly and/or agenesis of the corpus callosum (ACC) [1,2]. The 8q24.3 region is a site of copy-number variants (CNVs) associated with neurodevelopmental disorders [3]. For instance, patients with a large deletion on chromosome 8 show microcephaly and ACC [4], and a more specific deletion of the 8q24.3 region is associated with autism spectrum disorders (ASDs) or attention deficit hyperactivity disorders (ADHD) [5]. Additionally, duplication of the 8q24.3 region is associated with profound psychomotor retardation, idiopathic epilepsy and growth delay [6]. VRJS is considered as a contiguous gene syndrome because it results from the haploinsufficiency of the *SCRIB* and *PUF60* genes, which are both located within the minimal critical region [2]. While the idea that *PUF60* is the critical contributor of most of the phenotypes observed in this syndrome is gaining traction [2,7–14], the potential contribution of *SCRIB* to some of the observed structural and psychomotor deficits has not been assessed in mammals and is still a matter of debate. The best support for *Scrib* participating in VRJS came from morpholino-based knockdown experiments in zebrafish showing altered brain size in either *scrib* or *puf60* morphants [2]. Interestingly, a recent study reported the existence of a *PUF60-SCRIB* fusion transcript in a patient with 8q24.3 microdeletion and atypical VRJS [15].

Scribble (Scrib) is a conserved scaffold protein that acts as a hub for several signaling pathways and that functions in cell polarity during development [16,17]. In rodents, a homozygous *Scrib* mutation in a spontaneous mutant called *Circletail* (*Crc*) leads to early lethality accompanied by a severe form of neural tube defects (NTDs). Perturbation of *Scrib* in this mutant leads to major tissue polarity defects [18] that are hallmarks of planar cell polarity (PCP) signaling pathway deregulation [19], which can ultimately impact on the developing (and adult) nervous system [20–23]. Importantly, *Scrib* has been shown to participate in motor neuron migration [24], axonal guidance in

104 the hindbrain [25] and central nervous system myelination [26]. Additionally, our group
105 recently showed a role for *Scrib* in the brains of adult mice in fine tuning of excitatory
106 synapses and correlated its deletion with some features of ASDs [27–29]. In humans,
107 similar embryonic lethality and NTDs were reported for the *SCRIB* gene [30–32], and
108 microdeletions in 8q24.3 (encompassing both *PUF60* and *SCRIB*) were found in
109 children presenting microcephaly [2]. All these data suggest a role for *Scrib* in early
110 vertebrate brain development and call for further investigation.

111 To clearly establish the structural and psychomotor consequences of *Scrib*
112 deletion in the mammalian brain, we developed a conditional gene-targeting strategy to
113 generate three mouse lines [33]. The results showed that early deletion of *Scrib* in the
114 dorsal telencephalon recapitulated several neuroanatomical features observed in VRJS
115 patients, including reduced brain cortical size and agenesis of two commissural
116 bundles, including the corpus callosum (CC), while late deletion of *Scrib* in postmitotic
117 neurons resulted in mild cortical layering defects. Behavioral analysis of *Scrib* cKO
118 animals showed altered psychomotor behavior associated with memory deficits.
119 Altogether, our results show that the absence of *Scrib* during brain development
120 recapitulates some structural and behavioral deficits typical of VRJS, supporting a
121 molecular contribution of the gene to the pathology of this syndrome.

122

123 Results

124 *Scrib* expression is consistent with a developmental function in the forebrain

125 We evaluated the expression profile of Scrib in the developing brain using *in situ*
126 hybridization [27] and an in-house Scrib antibody for immunohistochemistry [34]. At
127 E16.5, *in situ* hybridization for Scrib indicated that it was expressed throughout the
128 dorsal forebrain and enriched in specific regions such as the upper layers of the cortical
129 plate (CP) along the medio-lateral axis (from the cingulate to the piriform cortex), in in
130 the sub-ventricular and ventricular zones (SVZ and VZ, respectively) and the Indusium
131 Griseum (IG) at the cortical midline **(Fig 1A-A'')**. Immunostaining confirmed this
132 expression pattern, with enrichment in the SVZ and VZ at cell-cell junctions in both
133 apical (labeled by Pals-1) and basal domains **(Fig 1B)**. At birth (day P0), Scrib is

colocalized with RC2+ radial glial cells in the cortex **(Fig 1C)** and it is also found in axonal tracts, especially in the interhemispheric commissural fibers such as the Ephrin-B2 positive fibers of the CC [35] **(Fig 1D)**. Double staining of Scrib (green) and GFAP (glial fibrillary acidic protein, a marker of mature glial cells, red) revealed that many cells among the midline glia are labeled for both markers **(Fig 1E)**.

Early *Scrib* deletion results in microcephaly and cortical layering defects

We crossed floxed *Scrib*$^{fl/fl}$ mice [29,36] with either *Emx1*-Cre mice, which express the Cre recombinase starting at E10.5 only in the dorsal telencephalic progenitors [37], or *FoxG1*-Cre mice, which express the Cre recombinase as early as E8.5 in the entire telencephalon [38] (hereafter reported as *Emx1-Scrib*$^{-/-}$ and *FoxG1-Scrib*$^{-/-}$ cKOs respectively). Specific *Scrib* excision in conditional mutants was validated **(Fig S1A-F)**, and the spatial expression pattern of Cre recombinase was further confirmed by crossing *Emx1-Scrib*$^{-/-}$ mice with the Ai6 reporter mice [39] **(Fig S1G-H)**. The cerebral hemispheres of *Emx1-Scrib*$^{-/-}$ cKOs were significantly smaller than those of their control littermates **(Fig 2A)**. Histological brain analysis at the rostral and caudal levels **(Fig 2B)**, revealed a pronounced decrease in the thickness of the caudal cerebral cortex (~25%) **(Fig 2C)**. This decrease was observed throughout the cingulate (Cg), motor (M), primary somatosensory (S1) and secondary somatosensory (S2) cortices and was maintained in adults (data not shown). This phenotype was absent in more rostral regions of *Emx1-Scrib*$^{-/-}$ cKO brains **(Fig 2D)**. *FoxG1-Scrib*$^{-/-}$ mutant brains displayed a similar but more severe reduction of cortical area and thickness along the entire rostrocaudal axis **(Fig S2A-D)**. We next examined the expression of markers of late-born neurons, such as Cuxl and Satb2 (layer II/III) and earlier-born neurons such as Ctip2 (layer V), some of these markers being essential to the formation of the CC [40,41]. In *Emx1-Scrib*$^{-/-}$ mutant P0 pups, we observed a reduction in the numbers of Cuxl-positive cells (ctrl, 28.2% ± 4.8; mutant, 18.5% ± 3.7; $p = 0.04$) and Satb2-positive cells (ctrl, 46.6% ± 2.4; mutant, 32.7% ± 3.5; $p = 0.002$), suggesting defects in cell fate **(Fig 2E-F)**. This was particularly pronounced in bins 2-4, corresponding to layers II-III. In contrast, the expression of Ctip2, a marker of early-born neurons, was unchanged

164 (ctrl, 22.3% ± 2.5; mutant, 19.1% ± 1.8; p = 0.24), but its cortical distribution was
165 altered: many Ctip2-positive neurons were mislocalized in the deeper layers of the
166 motor cortex (bins 8-10), implying migration defects **(Fig 2G)**. Notably, similar results
167 were observed within the somatosensory cortex (data not shown). A comparative
168 analysis in *FoxG1-Scrib*$^{-/-}$ mutant mice showed a more severe phenotype than that of
169 *Emx1-Scrib*$^{-/-}$ mutants, with a dramatic reduction in CuxI, Satb2 and Ctip2 expression
170 **(Fig S2E-G)**. These deficits probably arise from a combination of defects in cell fate and
171 migration, as depicted in **Fig 2H** and **S2H**. To confirm the role of *Scrib* in neuronal
172 migration, we used an approach based on *in utero* electroporation approach employing
173 a previously validated shRNA construct [27]. Scrib depletion resulted in a significant
174 increase in the fraction of electroporated cells mislocalized in the VZ/SVZ (ctrl shRNA,
175 5.4% ± 0.5; Scrib shRNA, 15% ± 1.4) associated with a significant decrease in the
176 fraction of cells reaching the upper layers (UL) (ctrl shRNA, 47.1% ± 1.4; Scrib shRNA,
177 30.7% ± 1.9) **(Fig 2I-J)**. Altogether, these results indicate that embryonic deletion of
178 *Scrib* reduces the size of the cortex, and alters the generation and positioning of the
179 cortical neurons, including callosal projection neurons (CPNs) in the upper layers of the
180 cortex.

181

182 **Early deletion of *Scrib* affects corpus callosum and hippocampal commissure**
183 **development**

184 Histological analysis was performed along the rostrocaudal axis in order to assess the
185 impact of early Scrib loss on the major forebrain commissure (the CC) but also the
186 dorsal and ventral hippocampal commissure (DHC and VHC) and the anterior
187 commissure (AC) [42] **(Fig S3A-B)**. Coronal histological sections of P0 *Emx1-Scrib*$^{-/-}$
188 mutant brains revealed ACC in caudal sections, with callosal axons apparently unable
189 to cross the midline **(Fig 3A-B)**. As in many mutant mouse models of ACC, failure of the
190 axons to cross was accompanied by large bundles of aberrantly projecting axons near
191 the midline, known as Probst bundles, which are frequently associated with hemispheric
192 fusion defects [43] **(Fig 3A'-B')**. Anterograde axonal tracing studies using DiI staining
193 confirmed the absence of midline-crossing callosal axons **(Fig 3A''-B'')**. In contrast,

194 callosal fibers in rostral sections from the brains of *Emx1-Scrib*$^{-/-}$ mice crossed the
195 midline despite an apparent thinning suggestive of CC hypoplasia **(Fig 3C-D'')**. Of note,
196 a similar phenotype was observed in adult *Emx1-Scrib*$^{-/-}$ mutant mice using 3D light-
197 sheet microscopy of uDISCO solvent-cleared brains [47] injected in the caudal cortex
198 with an adenovirus encoding GFP **(Fig 3E-F')** suggesting that ACC is not due to a
199 developmental delay. The deletion of *Scrib* in the *FoxG1*-Cre strain led to ACC along
200 the entire rostrocaudal axis **(Fig S4)**. Since *Scrib* is expressed in glial midline structures
201 **(Fig 1G)** that are critical for promoting hemisphere fusion and allowing the CC to cross
202 between hemispheres with the help of axonal guidance signals [44–46], we next sought
203 to determine whether CC agenesis observed in *Emx1-Scrib*$^{-/-}$ mutant mice may result
204 from mislocalization of glial structures. Immunostaining of P0 coronal sections at the
205 caudal level using antibodies against GFAP and the axonal marker L1-CAM revealed
206 that early deletion of Scrib resulted in a severe disorganization of the midline glia, with
207 GFAP-positive cells scattered along the dorsal part of the ventricle **(Fig 3G-H')**.
208 Parasagittal and horizontal brain sections of the *Scrib*$^{-/-}$ mutant confirmed the presence
209 of callosal defects **(Fig 4, S5)**. We found that the CC length was respectively reduced
210 by ~60% and ~40% in *FoxG1-Scrib*$^{-/-}$ and *Emx1-Scrib*$^{-/-}$ mutant mice, respectively,
211 compared with control littermates **(Fig 4A-C and S5A-C)**. Horizontal sections from P0
212 *Emx1-Scrib*$^{-/-}$ mutant mice confirmed the previously observed ACC and showed a
213 dramatic thinning of the DHC **(Fig 4D-E')**, a phenotype that was worsened in *FoxG1-*
214 *Scrib*$^{-/-}$ mice forming PB instead **(Fig S5D,E')**. In contrast, both *Scrib*$^{-/-}$ mutant mice lines
215 had relatively intact VHC **(Fig 4G' and S5G')** and AC (arrowheads in **Fig 4B and S5B)**.
216 3D imaging of adult *Emx1-Scrib*$^{-/-}$ mutant mice brains cleared with uDISCO injected in
217 the hippocampus with an adenovirus encoding mCherry, confirmed the absence of the
218 hippocampal commissure in adult animals **(Fig 4H-I')**. These findings indicate that early
219 and broad deletion of *Scrib* in the dorsal telencephalon (including the cerebral cortex
220 and the hippocampus) is responsible for the selective agenesis of the CC and dorsal
221 hippocampal commissure.
222

223 **Postmitotic deletion of *Scrib* affects cortical layering**

224 To specifically evaluate the effects of *Scrib* invalidation in postmitotic neurons, we
225 generated a third cKO mouse strain using mice expressing the Cre recombinase under
226 the *Nex* promoter around E11.5 in virtually every postmitotic excitatory neuron in the
227 forebrain [48,49] (these mice will be labeled hereafter as *Nex-Scrib*$^{-/-}$ mutant mice). After
228 proper characterization **(Fig S1A-C)**, we observed that *Nex-Scrib*$^{-/-}$ mutants showed no
229 obvious reduction of cortical area or thickness **(Fig 5A-B)**. Despite a mild CC
230 hypoplasia, *Nex-Scrib*$^{-/-}$ mutants display normal callosal fibers crossing the midline
231 either at the caudal **(Fig 5C-F)** which was consistent with normal glial midline structures
232 **(Fig 5G-H')**. Immunohistological analysis of the cortical layering in *Nex-Scrib*$^{-/-}$ mutant
233 mice revealed no major CPN production defects (see histograms in insets in **Fig 5I-K**).
234 However, the distribution of both early- and late-born neurons was affected with many
235 CPN mislocalized in deeper layers of the cortex at P0 (see arrowheads in **Fig 5I-K**).
236 These defects in layering are exemplified by the quantification of markers in bin 10
237 (deepest bin), showing an increase in CuxI- (ctrl, 0.6% ± 0.1; mutant, 17.3% ± 10.8; p =
238 0.046) **(Fig 5I)**, Satb2- (ctrl, 20.3% ± 4.6; mutant, 48.6% ± 17.3; p = 0.04) **(Fig 5J)**, and
239 Ctip2 percentages (ctrl, 12.2% ± 5.1; mutant, 43.7% ± 17.3; p = 0.04) **(Fig 5K)**, as
240 summarized in **Fig 5L**. These results highlight a late and cell-autonomous neuronal role
241 of *Scrib* in neuronal migration.

242

243 **Both early and late deletion of *Scrib* affect psychomotor development**

244 Since VRJS patients show altered psychomotor development, we next subjected our
245 mutant models with a variety of behavioral tests that required sensory-motor, emotional
246 and cognitive integration. We administered cortex-dependent tasks, including tests of
247 anxiety-like behavior, locomotor and exploratory activity, to adult *Emx1-Scrib*$^{-/-}$ and *Nex-*
248 *Scrib*$^{-/-}$ mice and their littermate controls (10–20 weeks). The most remarkable behavior
249 phenotype we observed was the effect on locomotor activity. Compared with their
250 controls, *Emx1-Scrib*$^{-/-}$ mutant mice showed significantly increased activity in a novel
251 environment, as measured by the distance traveled in the elevated plus-maze (*Emx1-*
252 *Scrib*$^{-/-}$ *vs*. *Ctrl*, *t*-test; t_{17} = 3.02, $p < 0.01$; **Fig 6A'**), open field (*Emx1-Scrib*$^{-/-}$ *vs*. *Ctrl*, *t*-

253 test; t_{17} = 2.35, $p < 0.05$; **Fig 6B'**) and Y maze (*Emx1-Scrib*$^{-/-}$ *vs*. *Ctrl*, *t*-test; t_{17} = 2.39, p
254 < 0.05; **Fig 6C'**) over the testing periods. In contrast, *Nex-Scrib*$^{-/-}$ mutant mice exhibited
255 significantly reduced exploration in the same tests, as the elevated plus-maze (*Nex-*
256 *Scrib*$^{-/-}$ *vs*. *Ctrl*, *t*-test; t_{24} = 2.55, $p < 0.05$; **Fig 6A''**), open field (*Nex-Scrib*$^{-/-}$ *vs*. *Ctrl*, *t*-
257 test; t_{25} = 2.13, $p < 0.05$; **Fig 6B''**) and Y maze (*Nex-Scrib*$^{-/-}$ *vs*. *Ctrl*, *t*-test; t_{24} = 3.09, $p <$
258 0.01; **Fig 6C''**). Another measure of spontaneous activity performed in a novel home
259 cage yielded similar results **(Fig 6D', 6D'')**. *Emx1-Scrib*$^{-/-}$ mutant mice were significantly
260 more active than their controls (genotype effect: $F_{1,143}$ = 8.757, $p < 0.05$; **Fig 6D'**)
261 whereas *Nex-Scrib*$^{-/-}$ mutant mice were significantly less active than their controls
262 (genotype effect: $F_{1,143}$ = 6.36, $p < 0.05$; **Fig 6D''**). In addition, nycthemeral locomotor
263 activity in their home cages was enhanced *in Emx1-Scrib*$^{-/-}$ mutant mice and lowered in
264 *Nex-Scrib*$^{-/-}$ mutant mice compared to the control mice, as determined by 24-hr
265 continuous monitoring of locomotor activity (p <0.05 for all genotype effect; **Fig**
266 **6D',6D''**). Notably, the *Emx1-Scrib*$^{-/-}$ and *Nex-Scrib*$^{-/-}$ mice did not display anxiety-like
267 behavior **(Fig S6B, S6C)** and no deficit was found in terms of balance or motor
268 coordination **(Fig 6E', 6E'', S6E, S6F)**. Considering that our models also had impaired
269 hippocampal and cortical connectivity, we assessed associative memory by testing
270 animals in the contextual fear-conditioning task, in which the animals have to associate
271 environmental cues with an electric shock [50]. All groups of mice were submitted to the
272 acquisition phase of the fear conditioning test **(Fig 6G)** and displayed a normal freezing
273 behavior with no reduction in pain tolerance **(Fig 6F)**. Mice were re-exposed to the
274 same environment 24 hr after training to evaluate the recent memory and 7 days after
275 training to evaluate the remote memory, which depends on the structural integrity of the
276 cortex **(Fig 6G', G'', H', H'')**. As classically observed, all groups of mice exhibited an
277 increase in freezing during the context and tone presentation tested at both 24-hr
278 (*Emx1-Scrib*$^{-/-}$ *vs*. *Ctrl*, context/cue effect: $F_{3,\ 55}$ = 23,28, p < 0,0001; *Nex-Scrib*$^{-/-}$ *vs*. *Ctrl*,
279 context/cue effect: $F_{3,\ 54}$ = 34,87, p < 0,0001; **Fig 6H**) and 7 days after training (*Emx1-*
280 *Scrib*$^{-/-}$ *vs*. *Ctrl*, context/cue effect: $F_{3,\ 55}$ = 28,16, p < 0,0001; *Nex-Scrib*$^{-/-}$ *vs*. *Ctrl*,
281 context/cue effect: $F_{3,54}$ = 49,38, p < 0,0001; **Fig 6I**). We found a deficit in cued remote
282 fear memory among *Emx1-Scrib*$^{-/-}$ mice, indicating a defect causing premature extinction
283 of cortex-dependent memory in this strain (*Emx1-Scrib*$^{-/-}$ *vs*. *Ctrl*, genotype effect: $F_{3,\ 55}$ =

284 10.18, p = 0,0024; Cue J7: t =2.924 p < 0.05; **Fig 6G'**), whereas recent memory was
285 unaffected (*Emx1-Scrib*$^{-/-}$ *vs*. *Ctrl*, no genotype effect: $F_{3, 55}$ = 1,646, p > 0,05; **Fig 6G'**).
286 In contrast, no difference was found in the recent (*Nex-Scrib*$^{-/-}$ *vs*. *Ctrl*, no genotype
287 effect: $F_{1, 54}$ = 0,0129, p > 0,05, **Fig 6G"**) or remote memory (*Nex-Scrib*$^{-/-}$ *vs*. *Ctrl*, no
288 genotype effect: $F_{1, 54}$ = 0,00016, p > 0,05, **Fig 6H"**) of *Nex-Scrib*$^{-/-}$ mice. Altogether,
289 these results suggest that *Emx1-Scrib*$^{-/-}$ mutant mice, in contrast to *Nex-Scrib*$^{-/-}$ mutant
290 mice, display hyperactivity in novel and familiar environments, which is compatible with
291 the altered psychomotor behavior observed in VRJS patients. In addition, the remote
292 memory deficits we observed in this mouse model may guide memory evaluation in
293 older VRJS patients.

294

295 **Discussion**

296 Our present study addresses the question of the participation of *Scrib* in some of the
297 structural and psychomotor phenotypes associated with Verheij/8q24.3 deletion
298 syndrome. Using several conditional mouse strains, we showed that early deletion of
299 *Scrib* leads to microcephaly and cortex layering defects associated with corpus
300 callosum and hippocampal commissure agenesis. Behavioral analysis of the same
301 mutants showed alterations in locomotor behavior accompanied by memory defects
302 which are reminiscent of the psychomotor defects observed in some VRJS patients.
303 Postmitotic deletion of *Scrib* in neurons resulted in mild layering defects that were also
304 associated with locomotor activity alterations. Our integrative neuroanatomical and
305 behavioral study of *Scrib*$^{-/-}$ mutant mice supports the participation of *Scrib* in
306 Verheij/8q24.3 deletion syndrome.

307

308 ***Scrib* deletion is associated with brain structural deficits consistent with**
309 **Verheij/8q24.3 deletion syndrome.**

310 Both mouse models with early deletion of *Scrib* (*FoxG1-Scrib*$^{-/-}$ and *Emx1*-Scrib$^{-/-}$ mutant
311 mice) display microcephaly in a range that is comparable to other well-established
312 microcephalic mouse models [51]. Our analysis shows that Scrib-dependent

313 microcephaly arises from a depletion in the neuronal lineage, as observed by a
314 decrease in CuxI- and Satb2-positive (layer II/III) CPNs, but also in Ctip2-positive (layer
315 V) CPNs, which is probably combined with migration defects. The late deletion of *Scrib*
316 in postmitotic glutamatergic neurons (*Nex-Scrib*$^{-/-}$ mutant mice*)* led to cortical layering
317 defects with mispositioned neurons from layers II/III and V, suggesting migration defects
318 that were validated by acute *Scrib* knockdown. Deficits in any of these critical
319 mechanisms (neurogenesis, cell fate, or migration) can participate in brain
320 malformation [52] and contribute to callosal neuron loss leading to abnormal
321 connectivity. From our data, we can suggest that the microcephaly observed in mutants
322 with embryonic *Scrib* deletion is most likely the result of a combination of disrupted
323 neurogenesis, cell fate and migration processes. This multifactor effect of *Scrib* is
324 consistent with its expression profile. We observed Scrib enrichment in the ventricular
325 zone (VZ) and sub-ventricular zone (SVZ) where it can contribute to asymmetric cell
326 division (ACD) and cell fate determination, as observed in other systems [53–55]. It is
327 also expressed in the cortex, including the radial glia, consistent with a role in migration.

328 The other phenotype we observed in the two mouse models with an early
329 deletion of Scrib was the CC and DHC agenesis. *Scrib* inactivation resulted in complete
330 ACC in both rostral and caudal domains in *FoxG1-Scrib*$^{-/-}$ cKOs, while *Emx1-Scrib*$^{-/-}$
331 cKOs display ACC only in the caudal part. The most likely explanation for this restricted
332 phenotype at the caudal level is that *Emx1* is expressed on a high-caudal to low-rostral
333 gradient [56,57]. In the rostral telencephalon, Scrib-dependent ACC is associated with
334 the formation of abnormal swirls of axons called Probst bundles [46]. Such a phenotype
335 is associated with failure of the callosal axons to cross the midline rather a problem with
336 outgrowth or guidance towards the midline. The expression of *Scrib* in the midline glia
337 and the observation of the disruption of the organization of that structure in *Emx1-Scrib*$^{-/-}$
338 mutant mice suggest that a *Scrib*-dependent non-autonomous mechanism affects the
339 crossing of the axons of the CC. Mutations in guidance cues expressed by the midline
340 glia typically lead to a Probst bundles phenotype; thus, we can envision that *Scrib*
341 deletion affects midline glial cells maturation and/or guidance cues secretion [42,44,45]
342 as seen in other systems [58,59]. Alternatively, these astroglial structures are essential
343 during interhemispheric remodeling that allows the crossing of callosal fibers [60].

344 Tissue fusion is central in the neural tube closure process [61], and PCP is a recurrent
345 theme in every tissue where fusion processes are extensively involved [62]. Finally, we
346 cannot completely exclude an autonomous role of *Scrib* in axon guidance as it was
347 shown to be important for axonal misrouting at the chiasm [63] and disrupts the
348 formation of spinal commissures in zebrafish [64], although the absence of CC or HC
349 deficits in the *Nex-Scrib*$^{-/-}$ mutant mouse model supports the hypothesis of a non-
350 autonomous effect.

351 Our results support the theory that the microcephaly and ACC observed in VRJS
352 patients could be the result, at least partially, of *Scrib* haploinsufficiency. Interestingly,
353 Edwards and collaborators discriminate two categories of human syndromes: on one
354 hand the ones that display only a microcephalic phenotype and, on the other hand, the
355 ones that do encompass both ACC and microcephaly [65]. We and others have shown
356 that several genetic mutations can result in complex neurodevelopmental disorders that
357 combine cortical alterations with ACC [66–69]. We believe that the human *SCRIB* gene
358 may also fall into this category: using different mouse models for *Scrib* invalidation, the
359 present work suggests and involvement in both microcephaly and ACC, reflecting a
360 possible concomitant function for this protein in cortical organization and axonal
361 guidance in the brain of VRJS patients during development.

362

363 ***Scrib* deficiency during embryogenesis leads to cognitive disabilities in adult**
364 **animals.**

365 Behavioral analysis of the *Scrib* cKO mice revealed alterations in psychomotor
366 behavior. Specifically, we observed hyperactive locomotor behavior when *Scrib* was
367 deleted embryonically (*Emx1-Scrib*$^{-/-}$ mutant mice) and hypoactive locomotor behavior
368 when *Scrib* was deleted postmitotically (*Nex-Scrib*$^{-/-}$ mutant mice) in every paradigm
369 tested (both in a novel and a familiar environment). These results strongly support a
370 critical role for *Scrib* in regulating locomotor behavior of the animal, but also highlight a
371 spatial and temporal dependence on *Scrib* regarding this regulation. Because of the
372 broad and early expression of *Emx1* in the brain, it is not possible to identify what region
373 drives the locomotor hyperactive behavior. On the other hand, *Nex* expression is

374 restricted to postmitotic glutamatergic neurons, supporting the hypothesis that the
375 pathological origin for the hypoactive locomotor behavior, also observed in some VRJS
376 patients, has a strict neuronal origin.

377 Exploration of cognitive performances shows that *Emx1-Scrib*$^{-/-}$, but not *Nex-*
378 *Scrib*$^{-/-}$ mutant mice, display memory deficit for a cortex-dependent remote-cued fear
379 memory recall. These results are interesting in light of the microcephaly and
380 commissural deficits present in the former but not the latter mutant. The CC primary
381 function is to integrate motor, sensory, and cognitive activity between the two
382 hemispheres [65,70]. The DHC provides interhemispheric connections between
383 hippocampi and despite few studies of the function of the DHC, one can envision that
384 the ability of the hippocampus to communicate effectively with contralateral homologous
385 regions via the DHC may be important for cognitive performance. Either this lack of
386 communication and/or the microcephaly and/or layering defects could be the cause of
387 these cognitive deficits. These results are in line with another study from our team that
388 revealed that loss of Scrib in postnatal excitatory hippocampal neurons (using *CaMKII-*
389 *Scrib*$^{-/-}$ mutant mice) led to an impaired hippocampus-dependent spatial memory [29].
390 Remarkably, the function of this pathway in the process of learning and memory seems
391 to extend toward the invertebrate phylum where *Scrib* is pivotal to the regulation of
392 active forgetting [71].

393 Considering the scarce number of VRJS patients, one can speculate that their
394 true phenotype spectrum may be wider than indicated by previous publications which
395 for the most part do not provide detailed neuropsychiatric evaluation. Neurological-
396 associated features for this syndrome include so far mild intellectual disability, delay of
397 developmental milestones such as standing upright and walking, delayed speech,
398 feeding issues and generalized seizures. All of these features, combined with
399 neuroanatomical features such as microcephaly and CC agenesis can fall under the
400 umbrella of a neurodevelopmental disorder whose affected individuals develop
401 psychomotor deficits reminiscent as those observed in ASDs, ADHD and schizophrenia.
402 Interestingly, a case for a male patient with ADHD revealed a chromosomal
403 translocation breakpoint at 8q24.3 has been reported [72] and this region appears to
404 overlap with ASDs as well [5]. From the molecular standpoint, glutamatergic

405 signalization is at the center of all attention for being a major player in these two
406 neurodevelopmental diseases [73]. Work from our group recently highlighted the
407 possibility that *Scrib*-impaired mice might be a model for studying synaptic dysfunction
408 and human psychiatric disorders such as ASDs [22,27], at least in part, by the
409 regulation of the glutamatergic signalization [28].

410 Most of the VRJS patients are fairly young individuals, and additional long-term
411 follow-up studies are needed, with special emphasis on locomotor hyper/hypoactivity
412 and cognitive dysfunction in these patients. Altogether, our results indicate that the
413 absence of *Scrib* during development causes the profound defects in the cortical
414 layering and interhemispheric connectivity that underlie cognitive disabilities.

415

416 ***Scrib* participation in other symptoms of VRJS**

417 The original report for Verheij syndrome described two patients with a multiorgan
418 developmental disorder characterized by features such as growth retardation,
419 dysmorphic facial features, feeding problems, cardiac ventricular septal defects,
420 coloboma and skeletal abnormalities [1]. Additional neurological features included
421 delayed psychomotor development, recurrent seizures with one patient who died early
422 of subdural hemorrhage and another who showed microcephaly, a hypoplastic CC and
423 delayed myelination. These observations were in line with previous observations of
424 patients with microcephaly, thin CC and intellectual disability mapping on 8q23.2-q24.12
425 [4]. In a subsequent landmark publication, Dauber et al. [2] reported 5 unrelated children
426 with 5 different heterozygous de novo interstitial deletions of chromosome 8q24.3. They
427 had global growth retardation, short stature and facial dysmorphism (5/5),
428 developmental delay and renal dysfunction (4/5) and microcephaly (3/5). More variable
429 features included vertebral abnormalities (3/5), coloboma and cardiac ventricular
430 defects (2/5) as well as seizures (1/5). The minimal common deletion found in patient #1
431 encompassed 3 genes including *SCRIB* and *PUF60* and displayed most of the cardinal
432 features of VRJS. Morpholino knockout of these genes in zebrafish, aimed at attributing
433 specific features to the loss of specific genes, showed that haploinsufficiency for *Scrib*
434 and *Puf60* was likely to contribute to the clinical features: knockdown of either *Puf60* or

435 *Scrib* recapitulated short stature, microcephaly, and reduced jaw size. *Scrib* knockdown
436 resulted in coloboma and renal abnormalities, while *Puf60* knockdown resulted in
437 cardiac defects. Knockdown of both genes exacerbated the short stature phenotype,
438 suggesting the possibility that the two genes may functionally interact [2]. Subsequent
439 studies in human genetics have mostly focused their attention on the *PUF60* gene as
440 the main driver of VRJS. In addition to 8q24.3 microdeletions, there have been 26
441 reported cases to date with CNVs in *PUF60* [2,7–14]. The most common phenotypes
442 observed in VRJS patients (for those tested) are recapitulated including developmental
443 delay/intellectual disability, facial dysmorphism and short stature (18/26), cardiac
444 defects (14/23), feeding difficulties (12/19), coloboma (9/26), and renal anomalies
445 (6/24). Importantly, although *PUF60* appears to be a major driver of these features of
446 VRJS syndrome, we noticed that neurological features were also reported, but in a
447 much lower proportions, such as microcephaly (8/26), CC hypoplasia/agenesis (4/26),
448 psychomotor alterations and seizure (3/26), indicating that *PUF60* CNVs are not the
449 main cause of these features.

450 The results of this study support a role for *Scrib* in some of the structural deficits
451 observed in VRJS patients. Our results also show psychomotor alteration when *Scrib* is
452 deleted, and we further identify cognitive disruption in our animal models. Additional
453 data from the literature suggest that *Scrib* could participate in extraneurological features
454 of VRJS. While most cardiac defects observed in VRJS patients are attributed to *PUF60*
455 deficiency, data from the Henderson laboratory show that both the *Scrib* spontaneous
456 mutant *Crc* and myocardium-specific *Scrib*$^{-/-}$ cKOs have ventricular septal defects and a
457 thinned myocardial wall that recapitulate cardiac features of VRJS patients [74,75] in
458 accordance with a fetal case carrying *SCRIB* haploinsufficiency [76]. In addition, a
459 recent exome sequencing analysis identified a rare nonsynonymous variants in *SCRIB*
460 that resulted in superior coloboma [77]. A common denominator that may explain the
461 defects observed after *SCRIB* loss such as neural tube defects, CC agenesis,
462 ventricular septal defects and coloboma, is a failure in the tissue fusion process [62]. In
463 addition to neural tube closure and interhemispheric fusion, it is important to note that
464 tissue fusion is essential to ventricular septal wall closure or to the formation of superior
465 ocular sulcus during eye formation and appears to depend on the PCP pathway and

466 *Scrib* [62,77]. *Scrib* deficiency may also explain the renal defects observed in VRJS
467 patients as the morpholino-based knockdown of *Scrib* in zebrafish impaired pronephros
468 development and induced cyst formation [78], while it appeared to be dispensable for
469 podocyte function and development [79].

470

471 **Concluding remarks**

472 Our findings uncover an essential role for *Scrib* in mammalian forebrain development
473 and connectivity, both of which ultimately affect animal behavior. Given that several
474 aspects of the neurological manifestations of the Verheij/8q24.3 syndrome were
475 recapitulated in our models, we suggest that *Scrib* may participate in human VRJS
476 syndrome. From the human genetics standpoint, any VRJS-related phenotype due to
477 *SCRIB* loss may prove difficult to observe because most mutations in human *SCRIB*
478 lead to severe neural tube defects so deleterious that they may obscure more "subtle"
479 phenotypes [30–32]. Further studies using models, including ours, are warranted in
480 order to determine whether other reproducible behavioral phenotypes such as reduced
481 seizure thresholds (i.e., seizure susceptibility) are also recapitulated in *Scrib*$^{-/-}$ cKOs.
482 While it is difficult to draw meaningful conclusions without analysis of additional patients
483 with 8q24.3 deletions, follow-up analyses in VRJS patients should systematically be
484 performed to determine whether ASDs and/or ADHD are underdiagnosed features of
485 VRJS patients. We suggest that rare *SCRIB* CNVs should be researched in the case of
486 VRJS patients who do not show *PUF60* CNVs. Altogether, our study demonstrates that
487 *Scrib*$^{-/-}$ mutant mice can provide an entry point to model representative contiguous gene
488 deletion syndrome such as VRJS.

489

490 **Materials and methods**

491 **Animal care and use**

492 All mice were housed in the animal facility of the Neurocentre Magendie, in
493 polypropylene cages under controlled conditions (at 23 ± 1 °C, with lights on from 7:00
494 A.M. to 7:00 P.M.). Food and water were available *ad libitum*. For timed pregnancy, the

495 morning in detection of vaginal plug was designated as embryonic day E0.5. This study
496 was performed according to the European Communities Council Directives
497 (2010/63/EU) and has been approved by the Animal Care and Use Committee
498 (Bordeaux) under the numbers 5012016-A and 5012015-A.

499 **Generation of brain-specific *Scrib* conditional knock-outs**

500 Scrib spontaneous mouse mutant *Circletail* causes severe brain and neural tube
501 damages that result in neonatal lethality [80], precluding the analysis of the role of *Scrib*
502 during forebrain development [27]. In order to circumvent this issue, we have applied a
503 conditional gene-targeting strategy to inactivate *Scrib* at different developmental stages
504 and in different cellular types in the brain. *FoxG1*-Cre, *Emx1*-Cre and the Cre reporter
505 mouse strain B6.Cg-*Gt(Rosa)26Sor*$^{tm6(CAG\text{-}ZsGreen1)Hze}$/J (Ai6) mice were purchased from
506 The Jackson Laboratory (Bar Harbor, ME). *Nex*-Cre mice were obtained from Klaus-
507 Armin Nave (Max Plank Institute, Germany). *Scrib*$^{fl/fl}$ floxed mice were generated
508 previously in collaboration with Neal Copeland, Nancy Jenkins and Rivka Rachel at
509 NIC/NIH [36]. *Scrib* mouse gene contains 38 exons that are translated into a full-length
510 180 kDa protein. In *Scrib*$^{fl/fl}$ floxed mice, lox-P sequences are inserted before exon 2
511 and after exon 8 [29]. When crossed with a mouse line expressing the Cre
512 recombinase, all the exons between 2 and 8 are excised, leading to the loss of the full
513 length protein. Heterozygous rodents were intercrossed to generate homozygous and
514 wildtype littermates as previously published [81]. *Scrib*$^{fl/fl}$ floxed mice were either
515 crossed with *FoxG1*-Cre, *Emx1*-Cre or *Nex*-Cre mice to obtain compound mice,
516 respectively referred to as *FoxG1-Scrib*$^{-/-}$, *Emx1-Scrib*$^{-/-}$ and *Nex-Scrib*$^{-/-}$ mutant mice
517 with early excision in different cellular types in the brain. All Scrib$^{-/-}$ cKO mice are viable,
518 fertile and do not display any gross physical abnormalities. Cre-mediated recombination
519 in *FoxG1*-Cre mice starts as early as E8.5 and occurs mostly in all cells from both
520 dorsal and ventral telencephalon [38]. This includes progenitors from neuroepithelium
521 that will specify various neuronal and glial cells from the neocortex and hippocampus,
522 but also from the ganglionic eminence that will give rise to GABAergic interneurons. In
523 *Emx1*-cre mice, the Cre recombinase is expressed later as compared with *FoxG1*-Cre
524 mice, starting as early as E10.5 and only in the dorsal telencephalon [37]. Emx1 pattern
525 of expression lead to the excision of *Scrib* in the vast majority of the neurons of the

526 neocortex and hippocampus, in glial cells of the pallium, but not in the GABAergic
527 interneurons. *Nex*-Cre mice express the Cre recombinase at or before E12.5 in the
528 hippocampus and in precursor cells in the VZ/SVZ, which eventually generate pyramidal
529 neurons that disperse throughout the cortex [48,49]. Most importantly for our study, Cre-
530 mediated recombination in *Nex*-Cre mice occurs neither in glial cells, oligodendrocytes
531 nor interneurons. Genotyping was performed as described previously by PCR using the
532 following primers: F (5'-gcacactgggtatcatggcta-3'), R1 (5'-gcaatctccagagccttacaga-3'),
533 R2 (5'-cccttggaaacctacatcccaa-3') [29]. Wild-type (WT), floxed, deleted *Scrib* alleles
534 were distinguished by the following amplified products: for WT band (F+R1; 437 bp),
535 flox band (F+R1; 541 bp) and cKO band (F+R2; 193 bp) **(Fig S1A)**. Cre genotyping was
536 performed using the following primers: F (5'-cggcatggtgcaagttgaata-3'), R (5'-
537 gcgatcgctattttccatgag-3'), resulting in a 300 bp band. Cre minus littermates showed no
538 detectable phenotype and were used as controls. The body weight of Emx1-Scrib$^{-/-}$ was
539 slightly lighter than their littermate controls (data not shown), which was not the case in
540 Nex-Scrib$^{-/-}$ mutant mice **(Fig S6A)**. It is worth noting that none of the *Scrib*$^{-/-}$ mutants
541 were homozygous for the knock-in Emx1-Cre allele (i.e., all were obligate Cre
542 heterozygotes), thus avoiding potential confounds related to Emx1 loss-of-function [82].
543 The Cre reporter mouse strain B6.Cg-*Gt(Rosa)26Sor*$^{tm6(CAG\text{-}ZsGreen1)Hze}$/J (Ai6) [39] which
544 expresses ZsGreen1 from the *Rosa26* locus, was used for evaluation of Emx1-Cre-
545 induced recombination efficiency. *Emx1-Scrib*$^{-/-}$ mice were crossed with Ai6 reporter
546 mice, resulting in enhanced green fluorescent protein (ZsGreen1) expression following
547 Cre-mediated recombination selectively in Emx1-expressing cells within the cortex,
548 hippocampus, fimbria and fibers within the caudate putamen **(Fig S1G-H)**. In contrast,
549 the striatum (ZsGreen1-negative) lacked Cre activity, consistent with Emx1 expression
550 pattern in the dorsal telencephalon.

551 **Histology, *in situ* hybridization analysis and Immunofluorescence**

552 For histology, heads (E16.5 embryos) or brains (P0 new-born) were harvested and fixed
553 in Bouin's or Carnoy's fixative (Electron Microscopy Sciences) overnight as previously
554 described [83]. Samples were dehydrated in ethanol, paraffin-embedded, and sectioned
555 (20 μm) coronally, horizontally or sagitally. Sections were collected onto Superfrost plus
556 Gold slides (Thermo Scientific), stained with hematoxylin and mounted with Entellan

557 (Millipore). The brains sections were examined using Leica MZ-16 stereomicroscope,
558 imaged in the Bordeaux Imaging Center (http://www.bic.u-bordeaux.fr) using the
559 NanoZoomer 2.0-HT slide scanner and analyzed using the Hamamatsu NDP viewer
560 software (Hamamatsu). For *in-situ* hybridization, E16.5 and E17.5 embryos brains were
561 dissected out, transferred in OCT solution and placed into the dry ice for storage at -
562 80°C before sectioning. *In situ* hybridization was performed using previously validated
563 digoxigenin-labeled cRNA probes [27]. 16 µm coronal embryonic brain sections of were
564 postfixed in 4% paraformaldehyde / 0.2% glutaraldehyde for 10 min at room
565 temperature (RT), bleached with 6% H2O2, digested in Proteinase K (5 µg/ml in PBS)
566 for 2.5 min and postfixed in 4% paraformaldehyde / 0.2% glutaraldehyde for 10 min at
567 RT. Then, slides were acetylated into freshly prepared 0.1M triethanolamine / PBS, pH
568 8, for 10 min at room temperature; 0.25% acetic anhydride acid was added for the last 5
569 min. Between each step, slides were rinsed with PBS. All subsequent steps were
570 performed as previously described in [27]. Images were acquired with Nanozoomer
571 (Hamamatsu). For immunofluorescence staining (IF), P0 pups were anesthetized with
572 pentobarbital, then perfused transcardially with 4% paraformaldehyde (PFA) in PB
573 buffer (0.1% PBS, 0.9% NaCl, PH = 7.4). Dissected brains were postfixed in 4% PFA
574 overnight at 4°C, infused in 30% sucrose in PB overnight and embedded in O.C.T
575 (Sakura Finetek). The OCT-embedded brains were cryosectioned coronally at a
576 thickness of 20 µm, mounted on Superfrost plus slides (VWR), washed with PBS, and
577 immunostaining was performed. Sections were hydrated with PBS, permeabilized with
578 0.2 % Triton-X100/PBS (PBS-T), blocked using 10% Normal Goat Serum (NGS) and
579 incubated overnight with the following primary antibodies in 5% NGS overnight at 4°C:
580 rabbit anti-GFAP (DAKO; 1:1000), rat anti-L1-CAM (Millipore; 1:1000), mouse anti-RC2
581 (DSHB; 1:100), rat Ctip2 (Abcam; 1:500), mouse Satb2 (Abcam; 1:100), rabbit Tbr1
582 (Millipore; 1:500), rabbit Cux1 (Santa Cruz Biotechnology; 1:100), rabbit anti-Scrib
583 (homemade AbMM468; 1:300) [34]. For Scrib immunostaining, brains were not perfused
584 but only briefly fixed in 4% PFA for 30 min. Samples were washed three times in PBS-T
585 and were incubated for 2 hr with the secondary antibodies Alexa Fluor® 488 or 546
586 Goat Anti-Mouse/Rat/Rabbit IgG (Life Technologies; 1:200) and then with DAPI (Life
587 Technologies; 1:20000) for 30 min. Finally, samples were washed three times in PBS

588 and mounted with Prolong Gold anti fading reagent (Invitrogen). Immunostained
589 sections were imaged at similar brain region using a Zeiss Axio Imager Z1 microscope
590 and Axio Vision (Version 4.7) imaging analysis software (Carl Zeiss). All images were
591 processed with Photoshop CS5 software (Adobe) and ImageJ software
592 (http://imagej.nih.gov).

593 **Quantitative analysis of laminar position in the cerebral cortex**

594 Sections chosen for analysis were matched along the rostral-caudal axis and observed
595 at the caudal level for every sample (where ACC is observed in Emx1-Scrib$^{-/-}$ cKO
596 brains). Immunofluorescence images were converted to gray values and normalized to
597 background staining. Regions of interest (ROIs) with a fixed width (but of variable
598 length, corresponding to the thickness of the cortex) were positioned in the motor cortex
599 region with the long axis perpendicular to the pial surface. Each ROI was subdivided
600 into ten equal bins from the pia (bin 1) to the outer border of the intermediate zone (bin
601 10) to assess CPN distribution across the layers of the cortex. In such arrangement,
602 layers II-III (Cux1- and Satb2-positive) were corresponding to bins 2-4 while layer V
603 (Ctip2-positive) was corresponding to bins 5-7 (highlighted in red in every figure). Slides
604 were evaluated blindly to the genotype and the number and distribution of CuxI-, Satb2-,
605 Ctip2- and DAPI-labeled cells in each zone was determined manually using the cell
606 counter plugin for ImageJ (http://rsbweb.nih.gov/ij/plugins/cell-counter.html). In order to
607 take into account a possible effect of Scrib deletion on total cell number in the cortex,
608 data are given as a ratio (in percent) of the total of cells positive for each marker to
609 DAPI-positive cells in each bin (mean ± SEM). Analysis was performed using at least 3
610 independent experiments (3 to 4 brains per genotype were quantified). The effect of the
611 genotype on the distribution of cells within the bins was assessed using the Student test
612 (*t test*).

613 **Callosal Axon tracing**

614 Corticocortical tract tracing was performed as previously described [84] using
615 fluorescent carbocyanine dye (1, 1′-Dioctadecyl-3, 3, 3′, 3′-
616 Tetramethylindocarbocyanine Perchlorate; DiI, Invitrogen). Brains were dissected at P0
617 and fixed in 4% PFA. A single DiI crystal was inserted in the dorsomedial cortex and

618 allowed to diffuse for 1 month. Coronal vibratome sections of 150 µm thickness were cut
619 on a vibratome, mounted on slides and imaged as described in the previous paragraph.

620 **UDisco**

621 Eight to ten-week old *Emx1-Scrib*$^{-/-}$ mice received unilateral stereotaxic microinjections
622 of a AAV (0.5/1µl at 300 nl per min) expressing GFP under the control of the promoter
623 hSyn1 (AAV9-hSyn1-GFP-2A-GFP-f, titer 4.8 x10^{12} GC/ml) in the sensory-motor cortex
624 region (anteroposterior [Y] -2 mm from Bregma, mediolateral [X] ± 1,2 mm, dorsoventral
625 [Z] -0,5 mm) or expressing mCherry under the control of the CamKII promoter (AAV2/9-
626 CamKII(0,4)-mcherry-WPRE, Vector Biolabs, titer 1.2 x1013 GC/ml) in the CA3 region
627 of hippocampus (anteroposterior [Y] -2 mm from Bregma, mediolateral [X] ± 3 mm,
628 dorsoventral [Z] -2,5 mm). Four weeks after surgery, the animals were perfused
629 transcardially with PB followed by 4% PFA in PBS; the brains were removed and
630 postfixed in 4% PFA for 24 hrs at 4°C and maintained in PBS. The entire brains were
631 cleared using the uDISCO technique as described [47]. The ultramicroscopy was
632 performed using the system from LaVision BioTec (Bielefeld, Germany) equipped with a
633 Fianium white laser, a sCMOS Andor camera, and a 0.5 NA 2X objective with a deeping
634 lens. A zoom from 0.63 to 6.3 could be applied. Images and 3D reconstruction were
635 analyzed with Image J and Imaris software.

636 **Western blot**

637 Cerebral cortices of P0 cKO pups and their control littermates were homogenized in
638 RIPA buffer (10 mM Tris-Cl (pH 8.0), 1 mM EDTA, 0.5 mM EGTA, 1% Triton X-100,
639 0.1% sodium deoxycholate, 0.1% SDS, 140 mM NaCl) supplemented with protease
640 inhibitor cocktail (Complete™; Roche). Protein concentration was determined using
641 Pierce BCA Protein assay kit (Thermo Scientific). Equal amounts of protein were diluted
642 in sample buffer, separated by sodium dodecyl sulfate–polyacrylamide gel
643 electrophoresis (SDS-PAGE), and visualized using the enhanced chemiluminescence
644 (ECL) as previously described [85]. Briefly, protein extracts were separated on an 8%
645 SDS-PAGE and transferred overnight to polyvinylidene difluoride membranes
646 (Millipore). Membranes were blocked with 5% nonfat milk in 1×Tris-buffered saline pH
647 7.4; 0.05% Tween-20 (TBS-T) for 30 min at room temperature (RT) and were probed

648 with homemade rabbit anti-Scrib (MM468; 1:500) [34] and mouse anti-GAPDH
649 (Millipore; 1:1000) for 1hr RT. Membranes were incubated with secondary antibodies
650 (GE Healthcare UK; donkey anti-rabbit or anti-mouse IgG conjugated to horseradish
651 peroxidase, 1:5000) in 1% nonfat milk in TBS-T for 1hr RT. Each incubation step was
652 followed by 3 washes with TBS-T for 10 min and immunoreactive signals were detected
653 using Pierce ECL substrate (Thermo Scientific). Band intensity was analyzed by
654 densitometry with the ImageJ software (http://imagej.nih.gov) and quantified as a
655 percentage of control band intensity using a representative of at least three independent
656 experiments.

657 ***In-utero* electroporation and tissue processing**

658 *In utero* electroporation experiments were performed according to protocols previously
659 described [86,87]. The Animal Care and Use Committee (Bordeaux) has approved the
660 experimental procedure under the number 5012015-A. Pregnant Swiss CD-1 mice were
661 anesthetized using 4 % isoflurane in an anesthesia induction chamber, maintained with
662 2 % isoflurane with an anesthetic mask and injected before surgery with buprenorphine.
663 Mice were subjected to abdominal incision; uterine horns were exposed and E14.5
664 embryos were placed on humidified gauze pads. Plasmid DNA was purified on Qiagen
665 columns (EndoFree Plasmid Maxi Kit), resuspended in sterile endotoxin-free buffers
666 (Qiagen) and mixed with Fast Green (Sigma). mCherry plasmid, together with pSuper or
667 validated pSuper-Scrib shRNA construct [27] were microinjected at a 1:3 ratio into the
668 lateral ventricles of embryos. Five current pulses (50 ms pulse / 950 ms interval; 35–36
669 V) were delivered across the heads of the embryos using 7 mm electrodes
670 (Tweezertrode 450165, Harvard Apparatus) connected to an electroporator (ECM830,
671 BTX). Surgical procedure was completed with suture of the abdomen wall and skin.
672 E18.5 embryos or P0 pups were processed for tissue analysis and immunostaining as
673 described in the histology section. Subregions of the cerebral cortex (VZ/SVZ, IZ, LL
674 and UL) were identified based on cell density using DAPI staining (Life Technologies;
675 1:20000). For each condition, sections from three embryos obtained from three
676 separate litters were quantified. Quantification of mCherry-positive cells was performed
677 using the cell counter plugin for ImageJ (http://rsbweb.nih.gov/ij/plugins/cell-

678 counter.html). Data are given as a percentage of the total of cells positive for mCherry in
679 each cortical subregion (mean ± SD).

680 **Behavioral testing**

681 Behavioral experiments were conducted with *Emx1-Scrib*$^{-/-}$ cKOs, *Nex-Scrib*$^{-/-}$ cKOs and
682 their control littermate male mice of 10–11 weeks of age at the start of behavioral tests.
683 All behavioral experiments were performed during the light phase (between 9:00 A.M.
684 and 7.00 P.M.) of a 12 h light/dark cycle, under conditions of dim light and low noise.
685 One week before starting the experiments, mice were housed in individual cage.
686 Several cohorts of animals and multiple behavioral tests were used. Whenever possible,
687 naïve animals were employed for behavioral testing; when the same cohort was used
688 for multiple tests, the most stressful essays were administered last, to minimize
689 between-test interference. To look for behavioral abnormalities mice were tested in
690 activity cages (to measure locomotor activity); in elevated plus maze, open field and Y-
691 maze (to measure exploratory activity and anxiety-like behavior); in rotarod, hot plate,
692 beam walking and grid handling test (to measure sensory-motor activity); and in the fear
693 conditioning test maze (to measure early and remote contextual end cued memory
694 performances). All experimental apparatuses were cleansed with hydroalcoholic
695 solution (Phagospray-DM) between subjects to remove odor residuals.

696 *Plus maze, Open field, Y maze and locomotor activity.* Elevated plus maze, Open field
697 and Y-maze experiments were performed as described previously [27,29]. Locomotor
698 activity in response to novelty and daily rhythm of activity experiments were performed
699 as described previously [27].

700 *Rotarod.* Mice performances on the rotarod, which accelerates from 4 to 40 rpm in 5
701 minutes, were evaluated for 5 trials per session on three consecutive days. A resting
702 time of 15 minutes was allowed between each trial. The end of a trial was considered
703 when mice were falling off the rod. Latency to fall was recorded for each trial. The
704 average latency was calculated for each testing day.

705 *Hot plate.* Animals were placed individually on a hot plate with the temperature adjusted
706 to 49°C.Response latency (sec) to jump or lick the hind paws was measured. The cut
707 off time was taken as 30 seconds to avoid risk of thermal injury to the skin.

Beam walking. During three successive days, mice were placed on one end of a wood beam (180 cm in length with a 2 or 1 cm square cross-section) at a height of 50 cm above a container with soft bedding and the time required to reach an enclosed safety box at the other end (80 cm away) is measured. On training day 1, beam was place horizontally and each mouse was trained to traverse the 2cm beam and then the 1cm beam. On training day 2, each mouse was trained to traverse the horizontal 1cm beam and then the 1cm beam inclined at an angle of 10° from ground. Tree training sessions par beam and the mice rest for 10 min in their home cages between training sessions on the two beams. On the day test, time taken to traverse the 1cm beam inclined at an angle of 10° from ground and the number of paw faults or slips are recorded. Analysis of each measure was based on the mean scores of the two best trials.

Grid handling. Mice were placed on a metal grid (spacing 1 cm2) and allowed to grip the grid with four paws. The grid was inverted at an angle of 180°, 20 cm above the ground and the time for the mouse to fall onto soft bedding was measured in seconds.

Fear conditioning. On day1, mice were trained in a standard fear conditioning apparatus. The training consisted of a single trial and was performed in a constantly illuminated Plexiglas cage (transparent walls and metal grid floor). Fear conditioning was performed by placing the mice in context A for 180s acclimation period followed by three conditional-unconditional stimulus (CS-US) separated by 120s interval. The CS-US consisted of 3 successive tones (CS, 20 s, 65 dB) and a footshock (US, 0.4 mA, 1 s, constant current) delivered through a stainless-steel grid floor. The fear conditioning chamber was thoroughly cleaned with 70% ethanol before each mouse was placed in the box. Memory for the context and the tone are evaluated on day 2 (recent memory) or 8 (remote memory) following conditioning. For the contextual memory test, mice are placed into the conditioning chamber and allowed to explore for 360 sec. For the tone memory test, mice are placed in a novel cage (cage with colored walls and flat plastic floor) 3 hr after the contextual memory test, allowed to acclimate to the chamber for 180sec and then presented with tone (180 sec, 65 dB). Freezing, an index of fear defined as the lack of movement except for heart-beat and respiration, was recorded during the 180sec acclimation period and context or tone presentation.

738 **Quantification, statistical analysis and data representation.**

739 Details of statistical analyses and n values are provided in the figure legends
740 subsections referring to individual assays. Statistical analyses were carried out using
741 the GraphPad Prism statistical package (GraphPad). Normality of distribution and
742 homogeneity of variance were validated and unpaired Student's two-tailed t-tests for two
743 data sets were used to compare groups with similar variance and are indicated along
744 the P values in figures. $P \leq 0.05$ was considered as statistically significant. Statistics were
745 derived from at least three independent experiments and not from technical replicates.
746 For behavior analyses, two-way ANOVA testing or repeated measure ANOVA was used
747 for the evaluation of the effect of genotype and time in actimetry, motor activation,
748 rotarod and fear conditioning behavioral test. The Bonferroni posthoc test was used
749 when appropriate. The Student's t-test was used for comparing genotype in other
750 behavior tests. Whenever adequate, individual data points were reported as
751 scatterplots to provide full information about the variability of data sets [88].

752

753 **Acknowledgements**: We thank Klaus-Armin Nave (Max Plank Institute, Germany) and
754 Neal Copeland, Nancy Jenkins (MD Anderson Cancer Center, USA) for providing *Nex*-
755 cre and *Scrib*$^{fl/fl}$ floxed mice respectively. We thank Anne Quiedeville, Chantal Médina
756 and Ronan Peyroutou for their technical assistance. We also thank the «animal and
757 genotyping facilities» members of the Neurocentre for technical assistance, notably
758 Helene Doat, Sara Laumond, Claire Lordan and Delphine Gonzales and co-workers, but
759 also the "Biochemistry and Biophysics Facility" of Bordeaux Neurocampus. We are
760 grateful to Christel Poujol and Sébastien Marais, members of the Bordeaux Imaging
761 Center (BIC, http://www.bic.u-bordeaux.fr), a service unit of the CNRS-INSERM and
762 Bordeaux University, member of the national infrastructure France BioImaging
763 supported by the French National Research Agency (ANR-10-INBS-04). These
764 research facilities are funded by the Labex B.R.A.I.N. (ANR-10-LABX-0043). We thank
765 Fatiha Boukhtouche and Peter Scheiffele for help with initial experiments using *in utero*
766 electroporation. We thank all members of the "Planar Polarity and Plasticity" team,
767 Fanny Mann and Valérie Castellani for thoughtful discussions.

768 **Author Contributions**

769 **Conceptualization:** Jerome Ezan, Maité M. Moreau, Nathalie Sans, Mireille
770 Montcouquiol

771 **Data Curation:** Jerome Ezan, Maité M. Moreau, Tamrat M. Mamo, Miki Shimbo,
772 Maureen Decroo, Melanie Richter, Froyland Calderon de Anda

773 **Formal Analysis:** Jerome Ezan, Maité M. Moreau, Tamrat M. Mamo, Miki Shimbo,
774 Maureen Decroo

775 **Funding Acquisition:** Jerome Ezan, Nathalie Sans, Mireille Montcouquiol

776 **Investigation:** Jerome Ezan, Maité M. Moreau, Tamrat M. Mamo, Miki Shimbo,
777 Maureen Decroo, Melanie Richter, Ronan Peyroutou, Froyland Calderon de Anda

778 **Methodology:** Jerome Ezan, Maité M. Moreau, Melanie Richter, Fadel Tissir, Froyland
779 Calderon de Anda, Nathalie Sans, Mireille Montcouquiol

780 **Project Administration:** Jerome Ezan, Fadel Tissir, Froyland Calderon de Anda,
781 Nathalie Sans, Mireille Montcouquiol

Resources: Jerome Ezan, Maité M. Moreau, Melanie Richter, Ronan Peyroutou, Rivka Rachel, Fadel Tissir, Froyland Calderon de Anda, Nathalie Sans, Mireille Montcouquiol

Supervision: Jerome Ezan, Fadel Tissir, Froyland Calderon de Anda, Nathalie Sans, Mireille Montcouquiol

Validation: Jerome Ezan, Maité M. Moreau, Tamrat M. Mamo, Miki Shimbo, Maureen Decroo, Melanie Richter, Froyland Calderon de Anda, Nathalie Sans, Mireille Montcouquiol

Visualization: Jerome Ezan, Maité M. Moreau

Writing – Original Draft Preparation: Jerome Ezan, Maité M. Moreau, Nathalie Sans, Mireille Montcouquiol

Writing – Review & Editing: Jerome Ezan, Maité M. Moreau, Tamrat M. Mamo, Miki Shimbo, Maureen Decroo, Fadel Tissir, Froyland Calderon de Anda, Nathalie Sans and Mireille Montcouquiol

Funding: This research was supported by INSERM, the French National Research Agency ANR NeuroScrib ANR-07-NEUR-031-01 (NS, MM), La Fondation pour la Recherche Médicale FRM grant #SPF20101221210 (JE) and « Equipe FRM » grant #DEQ20160334899 (MM), the European Commission Marie Curie Action CIG #303820 (JE), but also ERANET-NEURON (BMBF 01EW1910), JPND (BMBF 01ED1806), and Deutsche Forschungsgemeinschaft (DFG grant CA1495/4-1) (FCDA).The Montcouquiol/Sans lab is member of the Labex B.R.A.I.N. The funders had no role in study design, data collection and analysis, decision to publish, or preparation of the manuscript.

Competing interests: The authors declare no competing financial interests.

Correspondence and requests for materials should be addressed to mireille.montcouquiol@inserm.fr and/or jerome.ezan@inserm.fr

808 **Figures**

809

810 **Fig 1. Scrib expression in the mouse developing forebrain.**

811 **A-A'',** Representative *Scrib* expression pattern by ISH on E16.5 mouse embryo
812 sections. The dashed box in A are magnified in A' and A''. Scrib mRNA is detected on
813 the cortical plate (CP) in the subventricular zone (SVZ), the ventricular zone (VZ) and in
814 the indusium griseum (IG, arrows) and in ependymal cells (arrowheads) next to the
815 choroid plexus (CPx). MZ: marginal zone, IZ: intermediate zone. Scale bar: 0.5 mm (A)
816 and 0.1 mm (A'-A''). **B,** Representative Scrib (green) expression pattern by IF on E16.5
817 mouse embryo coronal sections. The dashed boxes in B are magnified in the inset.
818 Scrib protein is detected on the cortical plate (CP) but mostly in the SVZ and the VZ.
819 Higher magnification illustrates Scrib accumulation at cell-cell contacts in the entire VZ,
820 but no overlap with Pals-1 (red) apical marker. Scale bar: 0.1 mm (B). **C, D, E,**
821 Representative Scrib (green) expression pattern by IF on P0 cortex (C), Corpus
822 Callosum (CC) (D) and midline glia (E). Scrib labeling overlaps with RC2 (a marker of
823 radial glia, red in C), Ephrin-B2 (a marker of the CC, red in D) but also markedly
824 enriched in GFAP-positive (red in E) structures including the indusium griseum (IG) and
825 the midline zipper (MZ). Cg is the cingulate cortex. Higher magnification for selected
826 insets (boxed areas) illustrates strong Scrib expression in glial midline structures (see
827 arrowheads). Scale bar: 0.1 mm (E-G).

828

829 **Fig 2. Early deletion of *Scrib* leads to microcephaly associated with cortical**
830 **layering and neuronal migration defects. A**, Dorsal views of P0 *Emx1-Scrib*$^{-/-}$ cKO
831 mouse brains. Cortical plate areas are marked with a yellow dashed line for comparison
832 and quantification. Statistical analysis via a two-tailed t test (*$*P<0.05$*) using between 5
833 and 7 brains per genotype from at least 3 independent experiments. Error bars indicate
834 the SD. Scale bar: 1 mm. **B**, Schematic dorsal view of a P0 mouse brain that was
835 sectioned coronally and observed either at the rostral (R.) or caudal (C.) level as
836 indicated by the red dashed lines. **C-D**, Representative hematoxylin staining of coronal
837 sections from newborn *Emx1-Scrib*$^{-/-}$ cKO motor cortex at the caudal (C) and rostral (D)
838 levels and their respective controls. Note a marked reduction of the caudal motor cortex
839 thickness (M) in cKOs that extends to the cingulate (Cg) and somatosensory (S1-S2)
840 cortex. No major difference in cortical thickness was observed at the rostral level.
841 Cortical plate thickness was measured radially from the top of the upper layer (UL) to
842 the bottom of the lower layer (LL) of the cortex. IZ: intermediate zone, SVZ: sub-
843 ventricular zone, VZ: ventricular zone. Statistical analysis via a two-tailed t test
844 (*$**P<0.01, ***P<0.001$*) using 8 measurements per genotype from at least 3
845 independent experiments. Error bars indicate the SEM. Scale bar: 0.2 mm. **E-G**,
846 Representative immunofluorescence staining of CuxI (E), Satb2 (F) and Ctip2 (G) on
847 coronal sections from newborn *Emx1-Scrib*$^{-/-}$ cKO brains (orange) and their respective
848 controls (white) in the caudal motor cortex. Quantification of CuxI-, Satb2- and Ctip2-
849 positive neurons is shown as a percentage of total DAPI-positive cells (not shown) for
850 each ROI (see methods). In each ROI, layers II-III (Cux1- and Satb2-positive)
851 correspond to bins 2-4 while layer V (Ctip2-positive) corresponds to bins 5-7
852 (highlighted in red in every figure).The proportion of CuxI- and Satb2-positive late-born
853 neurons is decreased in *Emx1-Scrib*$^{-/-}$ cKO brains, while the Ctip2 percentage is
854 unchanged (see insets). Migration defects are suggested by the fact that several ectopic
855 Ctip2-positive cells are mislocalized in lowers, namely bins 8-10 (white arrowheads).
856 Statistical analysis via a two-tailed t test (*$*P<0.05, **P<0.01)$* using between 3 and 4
857 measurements per genotype from at least 3 independent experiments. Error bars
858 indicate the SD. **H**, Schematic representation of cortical layering in the caudal motor
859 cortex of *Emx1-Scrib*$^{-/-}$ cKO and its control. Early-born neurons (brown) are mislocalized,

860 while late-born neurons (blue) are decreased in proportion suggesting both migration
861 and cell fate defects after early loss of *Scrib* function. **I**, Cortical neurons were
862 electroporated *in utero* at E14.5 with an mCherry expressing vector together with control
863 shRNA or a previously validated Scrib shRNA. Brains were fixed at E18.5/P0. Nuclei
864 were stained with DAPI (blue) in order to delineate cortical subregions: dotted lines
865 represent boundaries between the upper layers (UL) and lower layers (LL) of the cortex,
866 the intermediary zone (IZ), the subventricular zone (SVZ) and the ventricular zone (VZ).
867 Arrowheads indicate either neurons reaching the upper layers of the cortex in the
868 control condition or Scrib shRNA-electroporated cells that remain in the deepest layers
869 of the cortex. **J,** Quantification of the distribution of mCherry-positive cells in distinct
870 subregions of the cerebral cortex for each condition (shRNA control, white bar; Scrib
871 shRNA, black bar) as shown in I. Analysis was performed using at least 3 independent
872 experiments. Error bars indicate SD. Statistical analysis via a two-tailed *t*-test (*$^{*}P<0.01$)
873 per condition from at least 3 independent experiments. See also Supplementary Fig S2.

874

875 **Fig 3. Partial corpus callosum agenesis in *Emx1-Scrib*$^{-/-}$ *cKO* mutants is**
876 **associated with impaired midline glia structure positioning. A-D**, Representative
877 hematoxylin staining of coronal sections from newborn *Emx1-Scrib*$^{-/-}$ cKO brains (B and
878 D) and their respective controls (A and C) at the caudal (A-B) or rostral (C-D) levels.
879 Dashed boxes in A-D are magnified in A'-D'. **A'-D'**, Higher magnification for selected
880 insets (boxed areas) from (A-D) illustrating high penetrance of CC agenesis (ACC) at
881 the caudal level. At P0, 93% of *Emx1-Scrib*$^{-/-}$ (n=28) cKO brains displayed ACC. Instead
882 of crossing the midline, CC axons formed whorls (Probst bundles, PB) on either side of
883 the midline that are indicated with an asterisk. Compared with control brains, a gap
884 between hemispheres indicates fusion defects. Despite an apparent thinning, CC fibers
885 do cross the midline at the rostral level. **A''-D''**, DiI crystals placed in the dorsomedial
886 cortex trace CC axons in *Emx1-Scrib*$^{-/-}$ cKO brains (B" and D") and their respective
887 controls (A" and C") at the caudal (A"-B") or rostral (C"-D") levels at P0. *Emx1-Scrib*$^{-/-}$
888 cKO$^{-/-}$ brains displayed occasional stalled fibers in some mutant brains (asterisk in B").
889 Abbreviations: cortex (Cx), hippocampus (Hp), corpus callosum (CC). The midline is
890 indicated as a white dashed line. **E-F'**, 3D imaging of adult brains cleared with uDISCO
891 from *Emx1-Scrib*$^{-/-}$ cKO brains (F and F', orange) and their respective controls (E and
892 E'). 3D reconstruction of the GFP expressed after viral infection in the sensory-motor
893 cortex are represented in yellow. In *Emx1-Scrib*$^{-/-}$ cKO brains, agenesis of the corpus
894 callosum is confirmed by the absence of cortical fibers passing through the contralateral
895 side (asterisk in F'). **G-H'**, Representative immunofluorescence staining of L1-CAM
896 (red) and GFAP (green) as a merged image (E and F) or GFAP only (E' and F', gray) on
897 coronal sections from newborn *Emx1-Scrib*$^{-/-}$ cKO brains (F and F', orange) and their
898 respective controls (E and E') at the caudal level. In *Emx1-Scrib*$^{-/-}$ cKO brains, agenesis
899 of the corpus callosum is confirmed by the failure of L1-CAM-positive axonal fibers to
900 cross the midline. GFAP-positive midline glial structures such as the MZ are missing in
901 these mutants, resulting in improper hemisphere fusion and failure for the IG to form
902 and localize appropriately. Scale bars: 1 mm in (A-D, E-F'), 0.1 mm in (A'-D', A"-C", G-
903 H). See also Supplementary Fig S4.

904 **Fig 4. ACC is accompanied by hippocampal commissure agenesis in *Scrib*$^{-/-}$ cKO**
905 **mutants. A-B**, Representative hematoxylin staining of para-sagittal sections from
906 newborn *Emx1-Scrib*$^{-/-}$ KO brains (B) and its control (A). Commissural plates are
907 magnified in each inset. The AC (indicated by arrowheads) is still present in brains from
908 cKO mutants. Scale bar: 1 mm (A) and 0.2 mm (B). **C**, Marked reduction of CC length
909 (arbitrary units, a.u.) along the rostrocaudal axis in the brains of *Emx1-Scrib*$^{-/-}$ cKO
910 brains (orange, n=5) as compared with those of their control littermates (orange, n=5).
911 Statistical analysis via a two-tailed *t*-test (****P<0.0001*) using between 3 and 5 brains
912 per genotype from at least 3 independent experiments. (indicated by an asterisk). **D-G**,
913 Representative hematoxylin staining of serial horizontal sections from newborn *Emx1-*
914 *Scrib*$^{-/-}$ (E, G) cKO brains and their respective controls (D, F) at the dorsal (D-E) and
915 ventral level (F-G). Dashed boxes in D-G are magnified in D'-G'. **D'-G'**, Higher
916 magnification for selected insets (boxed areas) from (D-G) illustrating agenesis of the
917 DHC (E') and CC hypoplasia (E',G'). Either dorsal (D'-E') or ventral (F'-G') sections
918 showed showed some callosal and hippocampal axon bundles still crossing through the
919 midline. **H-I'**, Light-sheet microscopy imaging of *Emx1-Scrib*$^{-/-}$ cKO adult brains (I) and
920 its control (H) cleared with uDISCO. 3D reconstruction of the mCherry expressed after
921 viral infection in the CA3 region of the hippocampus cortex is represented in yellow. The
922 HC (indicated by an arrowhead in control) is absent in brains from cKO mutants
923 (asterisk in I,I'). Scale bars: 1 mm in (A-B,D-G, H-I'), 0.2 mm in (D'-G'). See also
924 Supplementary Fig S5.

926 **Fig 5. Late deletion of *Scrib* specifically in postmitotic neurons does not**
927 **dramatically affect brain development. A**, Dorsal views of P0 *Nex-Scrib*$^{-/-}$ cKO mouse
928 brains. Cortical plate areas are marked with a yellow dashed line for comparison and
929 quantification. Statistical analysis via a two-tailed *t*-test using at least 5 brains per
930 genotype from at least 3 independent experiments. Error bars indicate the SEM. Scale
931 bar: 1 mm. **B**, Representative hematoxylin staining of coronal sections from newborn
932 *Nex-Scrib*$^{-/-}$ cKO motor cortex at the caudal level and its control. No significant reduction
933 of the caudal motor cortex thickness was observed in the mutant. Cortical plate
934 thickness was measured radially from the top of the upper layer (UL) to the bottom of
935 the lower layer (LL) of the cortex. IZ: intermediate zone, SVZ: subventricular zone, VZ:
936 ventricular zone. Statistical analysis via a two-tailed *t*-test using at least 5
937 measurements per genotype from at least 3 independent experiments. Error bars
938 indicate the SD. Scale bar: 0.2 mm. **C-D**, Representative hematoxylin staining of
939 coronal sections from newborn *Nex-Scrib*$^{-/-}$ cKO brains (D) and control brains (C) at the
940 caudal level. Dashed boxes in C-D are magnified in E-F. Scale bar: 1 mm. **E-F**, Higher
941 magnification for selected insets (boxed areas) from (C-D) illustrating the persistence of
942 corpus callosum in the *Nex-Scrib*$^{-/-}$ cKO brains. Scale bar: 0.1 mm. **G-H',** Representative
943 immunofluorescence staining of L1-CAM (red) and GFAP (green) as a merged image
944 (G and H) or GFAP only (G' and H', gray) on coronal sections from newborn *Nex-Scrib*$^{-/-}$
945 cKO brains (H and H', green) and their respective controls (G and G') at the caudal
946 level. GFAP-positive midline glia structures do form normally in *Nex-Scrib*$^{-/-}$ cKO
947 mutants. Scale bar: 0.1 mm. **I-K**, Representative immunofluorescence staining of CuxI
948 (I), Satb2 (J) and Ctip2 (K) on coronal sections from newborn *Nex-Scrib*$^{-/-}$ cKO brains
949 (green) and its control in the caudal motor cortex. Quantification of CuxI-, Satb2- and
950 Ctip2-positive neurons is shown as a percentage of total DAPI-positive cells (not shown)
951 for each ROI (see methods). In each ROI, layers II-III (Cux1- and Satb2-positive)
952 correspond to bins 2-4 while layer V (Ctip2-positive) corresponds to bins 5-7
953 (highlighted in red in every figure). The proportion of CuxI- and Satb2-positive late-born
954 neurons is decreased in *Emx1-Scrib*$^{-/-}$ cKO brains, while the Ctip2 percentage is
955 unchanged (see insets). Migration defects are suggested by the fact that several ectopic
956 Ctip2-positive cells are mislocalized in lower bins, namely bins 8-10 (white arrowheads).

957 Statistical analysis via a two-tailed *t*-test (**P<0.05, **P<0.01)* using between 3 and 4
958 measurements per genotype from at least 3 independent experiments. Error bars
959 indicate the SD. **L**, Schematic representation of cortical layering in the caudal motor
960 cortex of *Nex-Scrib*$^{-/-}$ cKO and its control. Early-born neurons (brown) are mislocalized,
961 while late-born neurons (blue) are decreased in proportion suggesting both migration
962 and cell fate defects after early loss of *Scrib* function.

963

964 **Fig 6. Psychomotor alterations and memory deficits in *Scrib*$^{-/-}$ cKO mutant mice.**
965 **A-H,** Behavioral responses in adult *Emx1-Scrib*$^{-/-}$ (orange) and *Nex-Scrib*$^{-/-}$ cKO mice
966 (green) as compared with their littermate control (white). **A-,** Spontaneous locomotor
967 activity. In the elevated plus maze test (A-A”), in the open field test (B-B”), in the Y-
968 maze (C-C”) and during exposure to a novel home cage (D-D”). While *Emx1-Scrib*$^{-/-}$
969 cKO mice travel longer distances than their respective controls (A’, B’, C’, D’), *Nex-*
970 *Scrib*$^{-/-}$ cKO mice display the opposite phenotype (A”, B”, C”, D”). The circadian profile
971 of the locomotor activity was measured in 1-hr increments during 24 hr in 12 hr light
972 (blocks 18 to 6) and 12 hr dark conditions (blocks 6 to 18). E-E”**,** Motor coordination. In
973 the rotarod test, no group of mice showed a deficit in coordination. F-F”, In a hot-plate
974 test, no group of mice showed a deficit in sensorimotor integration (F’). G-H**,** Percentage
975 of freezing measured before training (basal), 24 hours (24 hr) and 7 days (D7) after
976 training. In the cued fear conditioning test, *Emx1-Scrib*$^{-/-}$ cKO mice showed a profound
977 deficit in remote (D7) memory for the cued context when compared to control littermate
978 mice. Values are presented at means ± s.e.m. from 6-15 mice per genotype. *(*P<0.05,*
979 ***P<0.01)* versus control littermate group.

980

981

982

983 **Supplementary Figures**

984 **Supplementary Fig S1. Generation and characterization of *Scrib* conditional**
985 **knockout mouse mutants. A,** PCR genotyping to detect wild-type (437 bp), floxed
986 (541 bp) and targeted cKO (193 bp) alleles. *Cre*-mediated excision was confirmed in P0
987 pups cortices by the presence of a 300 bp product (lanes 3, 4 and 5). In the absence of
988 Cre, the wild-type and floxed alleles remain intact as determined by 437 and 541 bp
989 fragments, respectively (lane 1 and 2). When Cre-mediated recombination occurs
990 (lanes 3, 4 and 5), the floxed allele is excised, resulting in a 193 bp band, suggesting
991 efficient recombination. **B,** Schematic representation of the genomic organization of
992 mouse *Scrib* gene with 38 exons (solid boxes) including exons encoding for LRR (green
993 boxes) or PDZ (purple boxes) domains of the protein. Cre recombinase-based excision
994 of exons 2-8 leads to the expression of an unstable truncated protein of 135KDa (see
995 methods). **C,** Representative western blots from control and *Scrib*$^{-/-}$ cKO cerebral
996 cortices showing full-length (180 KDa) Scrib protein. Cortical protein extracts of P0
997 *FoxG1-Scrib*$^{-/-}$, *Emx1-Scrib*$^{-/-}$ and *Nex-Scrib*$^{-/-}$ cKOs were immunoblotted with anti-Scrib
998 MM468 antibody and anti-GAPDH as a control. cKO lysates (lanes 2, 4 and 6) show
999 reduced levels of Scrib when compared with control littermates (lanes 1, 3 and 5). **D,**
1000 Histograms summarizing western blot quantification (densitometric intensity values). In
1001 the cKOs, the protein levels are variably reduced (from strong to moderate depending
1002 on the Cre line considered), with residual expression most likely derived from glia, blood
1003 vessels and tissue that do not express the Cre recombinase. Statistical analysis via a
1004 two-tailed t test (*P**<0.001, P***<0.0001*) using between 4 and 8 cortical samples per
1005 genotype from at least 3 independent experiments. Error bars indicate the SEM. **E,**
1006 Scrib expression on coronal cryosection of P0 *Emx1-Scrib*$^{-/-}$ cKOs mutants and control
1007 littermates. Comparison of Scrib immunostaining shows dramatic decrease in the level
1008 of Scrib protein expression in cortex and hippocampus. Negligible labeling of Scrib in
1009 *Emx1-Scrib*$^{-/-}$ cKOs mutants cortex (Cx), hippocampus (Hp) and fimbria (area
1010 surrounded by yellow dashed line) verify the specificity of the Scrib antibody.
1011 Persistence of Scrib expression in the ventro-medial structures verifies the specificity of
1012 the excision (see star *). Scale bar: 0.5mm. **F,** Higher magnification insets for the Hp
1013 and Cx areas from E. Scale bar: 0.1mm. **G-H,** P0 coronal sections of *Emx1-Scrib*$^{-/-}$*-Ai6*

1014 mouse brains. By crossing *Emx1-Scrib*$^{-/-}$ into a Ai6 reporter mouse strain, we confirmed
1015 the Emx1-driven expression of the Cre recombinase in Cx, Hp and fimbria (Fi). Both
1016 rostral (G) and caudal (H) sections show robust ZSGreen1 expression in the dorsal
1017 forebrain, thus assessing efficient recombination, while the striatum show almost no
1018 sign of Cre−mediated recombination (see star *). Scale bar: 0.5mm.

1019

1020 **Supplementary Fig S2. Early deletion of *Scrib* leads to microcephaly. Cortical**
1021 **layering is severely disturbed in *FoxG1-Scrib*$^{-/-}$ cKO brains. A**, Dorsal views of P0
1022 *FoxG1-Scrib*$^{-/-}$ cKO mice brains. Cortical plate areas are marked with a yellow dashed
1023 line for comparison and quantification. Statistical analysis via a two-tailed t test
1024 (*P*<0.05*) using between 5 and 8 brains per genotype from at least 3 independent
1025 experiments. Error bars indicate the SD. Scale bar: 1 mm. **B**, Schematic dorsal view of
1026 a P0 mouse brain that were sectioned coronally and observed either at the rostral (R.)
1027 or caudal (C.) level as indicated by the red dashed lines. **C-D**, Representative
1028 hematoxylin staining of coronal sections from newborn *FoxG1-Scrib*$^{-/-}$ cKO motor cortex
1029 at the caudal (C) and rostral (D) levels and their respective controls. Note a marked
1030 reduction of the motor cortex thickness (M) in cKOs that extends to the cingulate (Cg)
1031 and somatosensory (S1-S2) cortex at both rostral (C) and caudal (D) levels. Cortical
1032 plate thickness was measured radially from the top of the upper layer (UL) to the bottom
1033 of the lower layer (LL) of the cortex. IZ: Intermediate Zone, SVZ: Sub-Ventricular Zone,
1034 VZ: Ventricular Zone. Statistical analysis via a two-tailed t test (*P***<0.0001*) using
1035 between 6 to 8 measurements per genotype from at least 3 independent experiments.
1036 Error bars indicate the SEM. Scale bar: 0.2 mm. **E-G**, Representative
1037 Immunofluorescence staining of CuxI (E), Satb2 (F) and Ctip2 (G) on coronal sections
1038 from newborn *FoxG1-Scrib*$^{-/-}$ cKO brains (dark red) and their respective controls (red) in
1039 caudal motor cortex. Quantification of CuxI-, Satb2- and Ctip2-positive neurons is
1040 shown as a percentage of total DAPI-positive cells (not shown) for each ROI (see
1041 methods). In each ROI, layers II-III (Cux1- and Satb2-positive) are corresponding to
1042 bins 2-4 while layer V (Ctip2-positive) is corresponding to bins 5-7 (highlighted in red in
1043 every figure). Severe reduction of CuxI (ctrl, 29.9% ± 3.4; mutant, 9.75% ± 2.3; p =
1044 0.003), Satb2 (ctrl, 40.5% ± 2.2; mutant, 17.9% ± 2.4; p = 0.001) and Ctip2 (ctrl, 11.4%
1045 ± 0.8; mutant, 6.1% ± 0.9; p = 0.006) percentages were observed in *FoxG1-Scrib*$^{-/-}$ cKO
1046 caudal motor cortices. A few Ctip2-positive cells were also found in deeper layers of the
1047 cortex, suggesting migration defects in addition to potential neurogenesis impairment.
1048 Statistical analysis via a two-tailed t test (*P*<0.05, P**<0.01)* using between 3 to 4
1049 measurements per genotype from at least 3 independent experiments. Error bars
1050 indicate the SD. **H**, Schematic representation of cortical layering in caudal motor cortex

1051 of *FoxG1-Scrib*$^{-/-}$ cKO and its control. Both early-born (brown) and late-born neurons
1052 (blue) are massively decreased in proportion suggesting cell fate defects after *Scrib*
1053 early invalidation in this cKO strain. See also Fig 5.See also Fig3.

1054

1055 **Supplementary Fig S3. Schematic representation of section through the**
1056 **commissural plate.**

1057 **A**, Schematic para-sagittal depiction of a P0 mouse brain commissural plate. **B**, Higher
1058 magnification of the commisural plate (green) from (A) depicting the Corpus Callosum
1059 (CC in purple), the Dorsal Hippocampal Commissure (DHC in yellow), the Ventral
1060 Hippocampal Commissure (VHC in blue) and the Anterior Commissure (AC in brown).
1061 Brains sections were observed either caudally (C.) or rostrally (R.) along the rostro-
1062 caudal axis as indicated by the red dashed lines. Relative to Figure 3, 5 and S4. **C-D,**
1063 Schematic para-sagittal view of a P0 mouse brain. Brains were sectioned either para-
1064 sagitally (Ps. in C) or horizontally (in D) as indicated by the red dashed line. (D), Higher
1065 magnification of the commisural plate (green) from (C) depicting the Corpus Callosum
1066 (CC in purple), the Dorsal Hippocampal Commissure (DHC in yellow), the Ventral
1067 Hippocampal Commissure (VHC in blue) and the Anterior Commissure (AC in brown).
1068 CC length (L.) was determined as indicated by the red bracket. Brains were sectioned
1069 either para-sagitally (C) or horizontally along the dorso-ventral axis (D) and were
1070 observed either at the dorsal (D.) or ventral (V.) level as indicated by the red dashed
1071 lines. Relative to Fig 4 and S5.

1072

1073 **Supplementary Fig S4. Complete corpus callosum agenesis in *FoxG1-Scrib*$^{-/-}$ *cKO***
1074 **mutants. A**, Schematic para-sagittal depiction of a P0 mouse brain commissural plate.
1075 **B**, Higher magnification of the commisural plate (green) from (A) depicting the Corpus
1076 Callosum (CC in purple), the Dorsal Hippocampal Commissure (DHC in yellow), the
1077 Ventral Hippocampal Commissure (VHC in blue) and the Anterior Commissure (AC in
1078 brown). Brains sections were observed either caudally (C.) or rostrally (R.) along the
1079 rostro-caudal axis as indicated by the red dashed lines. **C-F**, Representative
1080 hematoxylin staining of coronal sections from newborn *FoxG1-Scrib*$^{-/-}$ cKO brains (D and
1081 F) and their respective controls (C and E) at the caudal (C-D) or rostral (E-F) levels.
1082 Dashed boxes in C-F are magnified in C'-F'. **C'-F'**, Higher magnification for selected
1083 insets (boxed areas) from (C-F) illustrating high penetrance of CC agenesis (ACC) both
1084 at the caudal and rostral level. At P0, 100% of *FoxG1-Scrib*$^{-/-}$ (n=12) cKO brains
1085 displayed ACC. Instead of crossing the midline, CC axons formed whorls (Probst
1086 bundles, PB) on either side of the midline that are indicated with an asterisks in D' and
1087 F'. **C''-F''**, DiI crystals placed in the dorsomedial cortex trace CC axons in *FoxG1-Scrib*$^{-/-}$
1088 cKO brains (D" and F") and their respective controls (C" and E") at the caudal (C"-D") or
1089 rostral (E"-F") levels at P0. In *FoxG1-Scrib*$^{-/-}$ cKO brains, misrouted callosal axons form
1090 dense PB (asterisks in D", F") lateral to the midline. Abbreviations: Cortex (Cx),
1091 Hippocampus (Hp), Corpus Callosum (CC). Midline is indicated as a white dashed line.
1092 Scale bars: 1 mm in (C-F), 0.1 mm in (C'-F'). See also Fig3.

1093

1094 **Supplementary Fig S5. ACC is accompanied by hippocampal commissure**
1095 **agenesis in *Scrib*$^{-/-}$ cKO mutants. A-B,** Schematic dorsal (A) or para-sagittal (B) views
1096 of a P0 mouse brain. Brains were sectioned either para-sagitally (Ps. in A) or
1097 horizontally (in B) as indicated by the red dashed line. **C**, Higher magnification of the
1098 commisural plate (green) from (B) depicting the Corpus Callosum (CC in purple), the
1099 Dorsal Hippocampal Commissure (DHC in yellow), the Ventral Hippocampal
1100 Commissure (VHC in blue) and the Anterior Commissure (AC in brown). CC length (L.)
1101 was determined as indicated by the red bracket. Brains were sectioned either para-
1102 sagitally (D-F) or horizontally (G-J') along the dorso-ventral axis and were observed
1103 either at the dorsal (D.) or ventral (V.) level as indicated by the red dashed lines. **D-E**,
1104 Representative hematoxylin staining of para-sagittal sections from newborn *FoxG1-*
1105 *Scrib*$^{-/-}$ KO brains (E) and its control (D). Commissural plates are magnified in each
1106 inset. The AC (indicated by arrowheads) is still present in brains from cKO mutants. **F**,
1107 Marked reduction of CC length (arbitrary units a.u) along the rostro-caudal axis in
1108 *FoxG1-Scrib*$^{-/-}$ cKO brains (red, n=8) as compared with their control littermates (white,
1109 n=6). Statistical analysis via a two-tailed t test (*P***<0.0001*) using between 5 and 8
1110 brains per genotype from at least 3 independent experiments. **H-O**, Representative
1111 hematoxylin staining of serial horizontal sections from newborn *FoxG1-Scrib*$^{-/-}$ (I,M) and
1112 *Emx1-Scrib*$^{-/-}$ (K,O) cKO brains and their respective controls (H,L,J,N) at the dorsal (H-
1113 K) and ventral level (L-O). Dashed boxes in H-O are magnified in H'-O'. **G-J**,
1114 Representative hematoxylin staining of serial horizontal sections from newborn *FoxG1-*
1115 *Scrib*$^{-/-}$ (H, J) cKO brains and their respective controls (G, I) at the dorsal (G-H) and
1116 ventral level (I-J). Dashed boxes in G-J are magnified in G'-J'. **G'-J'**, Higher
1117 magnification for selected insets (boxed areas) from (G-J). Sections through the *FoxG1-*
1118 *Scrib*$^{-/-}$ cKO brains reveal the complete absence of the CC and DHC. Misrouted callosal
1119 axons form dense PB (asterisks) lateral to the midline in dorsal sections (H') and failed
1120 to reach the contolateral hemisphere ventrally (J', asterisk). Despite an apparent
1121 thinning, the VHC is still observed in ventral sections (J').These defects were penetrant
1122 in all *Scrib*$^{-/-}$ cKO mutants observed (n=3 for each genotype). Scale bars: 1 mm in (C-F,
1123 H-O), 0.2 mm in (H'-O'). See also Fig4.

1124

1125 **Supplementary Fig S6. Genetic deletion of *Scrib* in mice does not induce anxious**
1126 **or neophobic behavior and does not affect balance and motor coordination. A-F,**
1127 Behavioral responses in adult *Emx1-Scrib*$^{-/-}$ cKO mice (orange) and adult *Nex-Scrib*
1128 cKO mice (green) as compared with their control littermate. **A,** Body weight of adult
1129 mice. **B,** Time spent in open arms during 5min in the elevated plus maze. Compared to
1130 the control littermate, all mutant mice spent a normal amount of time in the open to total
1131 arms (*t*-test; *Emx1 vs*. Ctrl, t_{19}=1.15; *Nex vs*. Ctrl, t_{25}=1.17; all n.s). **C,** Time in center of
1132 the open field during 5 min. Consistently, all mutant mice spent a comparable amount of
1133 time in the center region of the open field area, as compared with WT mice (*t*-test; *Emx1*
1134 *vs*. Ctrl, t_{20}=0.06; *Nex vs*. Ctrl, t_{26}=0.76; all n.s). **D,** Total number of entry in Y maze
1135 during 5min. In experiments exploring neophobia, both Scrib mutant mice displayed
1136 normal spontaneous spatial novelty preference in the Y maze test indicated by
1137 comparable number of arms entries than controls mice (*t*-test; *Emx1 vs*. Ctrl, t_{20}=1.02;
1138 *Nex vs*. Ctrl, t_{25}=1.41; all n.s). **E**, Total spent time (right panel), velocity (middle panel)
1139 and number of flips (left panel) during the beam walking test. **F**, Measured of latency to
1140 fall during the grid handling test. Values are presented at means ± SEM from 8–14 mice
1141 per genotype.

1142

1143 ## References

1144 1. Verheij JBGM, de Munnik SA, Dijkhuizen T, de Leeuw N, Olde Weghuis D, van den Hoek GJ, et al. An
1145 8.35 Mb overlapping interstitial deletion of 8q24 in two patients with coloboma, congenital heart
1146 defect, limb abnormalities, psychomotor retardation and convulsions. Eur J Med Genet. 2009;52:
1147 353–357. doi:10.1016/j.ejmg.2009.05.006

1148 2. Dauber A, Golzio C, Guenot C, Jodelka FM, Kibaek M, Kjaergaard S, et al. SCRIB and PUF60 are
1149 primary drivers of the multisystemic phenotypes of the 8q24.3 copy-number variant. Am J Hum
1150 Genet. 2013;93: 798–811. doi:10.1016/j.ajhg.2013.09.010

1151 3. Iyer J, Girirajan S. Gene discovery and functional assessment of rare copy-number variants in
1152 neurodevelopmental disorders. Brief Funct Genomics. 2015;14: 315–328. doi:10.1093/bfgp/elv018

1153 4. Halevy A, Basel-Vanagaite L, Shuper A, Helman S, Har-Zahav A, Birk E, et al. Microcephaly-thin
1154 corpus callosum syndrome maps to 8q23.2-q24.12. Pediatr Neurol. 2012;46: 363–368.
1155 doi:10.1016/j.pediatrneurol.2012.03.014

1156 5. Stam AJ, Schothorst PF, Vorstman JA, Staal WG. The genetic overlap of attention deficit
1157 hyperactivity disorder and autistic spectrum disorder. Appl Clin Genet. 2009;2: 7–13.

1158 6. Bonaglia MC, Giorda R, Tenconi R, Pessina M, Pramparo T, Borgatti R, et al. A 2.3 Mb duplication of
1159 chromosome 8q24.3 associated with severe mental retardation and epilepsy detected by standard
1160 karyotype. Eur J Hum Genet. 2005;13: 586–591. doi:10.1038/sj.ejhg.5201369

1161 7. El Chehadeh S, Kerstjens-Frederikse WS, Thevenon J, Kuentz P, Bruel A-L, Thauvin-Robinet C, et al.
1162 Dominant variants in the splicing factor PUF60 cause a recognizable syndrome with intellectual
1163 disability, heart defects and short stature. Eur J Hum Genet. 2016;25: 43–51.
1164 doi:10.1038/ejhg.2016.133

1165 8. Low KJ, Ansari M, Abou Jamra R, Clarke A, El Chehadeh S, FitzPatrick DR, et al. PUF60 variants cause
1166 a syndrome of ID, short stature, microcephaly, coloboma, craniofacial, cardiac, renal and spinal
1167 features. Eur J Hum Genet. 2017;25: 552–559. doi:10.1038/ejhg.2017.27

1168 9. Santos-Simarro F, Vallespin E, Del Pozo A, Ibañez K, Silla JC, Fernandez L, et al. Eye coloboma and
1169 complex cardiac malformations belong to the clinical spectrum of PUF60 variants. Clin Genet.
1170 2017;92: 350–351. doi:10.1111/cge.12965

1171 10. Graziano C, Gusson E, Severi G, Isidori F, Wischmeijer A, Brugnara M, et al. A de novo PUF60
1172 mutation in a child with a syndromic form of coloboma and persistent fetal vasculature. Ophthalmic
1173 Genet. 2017;38: 590–592. doi:10.1080/13816810.2017.1318927

1174 11. Zhao JJ, Halvardson J, Zander CS, Zaghlool A, Georgii-Hemming P, Månsson E, et al. Exome
1175 sequencing reveals NAA15 and PUF60 as candidate genes associated with intellectual disability. Am
1176 J Med Genet B Neuropsychiatr Genet. 2018;177: 10–20. doi:10.1002/ajmg.b.32574

1177 12. Moccia A, Srivastava A, Skidmore JM, Bernat JA, Wheeler M, Chong JX, et al. Genetic analysis of
1178 CHARGE syndrome identifies overlapping molecular biology. Genet Med. 2018;20: 1022–1029.
1179 doi:10.1038/gim.2017.233

1180 13. Xu Q, Li C-Y, Wang Y, Li H-P, Wu B-B, Jiang Y-H, et al. Role of PUF60 gene in Verheij syndrome: a case
1181 report of the first Chinese Han patient with a de novo pathogenic variant and review of the
1182 literature. BMC Med Genomics. 2018;11: 92. doi:10.1186/s12920-018-0421-3

1183 14. Alkhunaizi E, Braverman N. Clinical characterization of a PUF60 variant in a patient with Dubowitz-
1184 like syndrome. Am J Med Genet A. 2019;179: 130–133. doi:10.1002/ajmg.a.60691

1185 15. Abdin D, Rump A, Tzschach A, Sarnow K, Schröck E, Hackmann K, et al. PUF60-SCRIB fusion
1186 transcript in a patient with 8q24.3 microdeletion and atypical Verheij syndrome. Eur J Med Genet.
1187 2018; doi:10.1016/j.ejmg.2018.11.021

1188 16. Stephens R, Lim K, Portela M, Kvansakul M, Humbert PO, Richardson HE. The Scribble Cell Polarity
1189 Module in the Regulation of Cell Signaling in Tissue Development and Tumorigenesis. J Mol Biol.
1190 2018; doi:10.1016/j.jmb.2018.01.011

1191 17. Bonello TT, Peifer M. Scribble: A master scaffold in polarity, adhesion, synaptogenesis, and
1192 proliferation. J Cell Biol. 2019;218: 742–756. doi:10.1083/jcb.201810103

1193 18. Montcouquiol M, Rachel RA, Lanford PJ, Copeland NG, Jenkins NA, Kelley MW. Identification of
1194 Vangl2 and Scrb1 as planar polarity genes in mammals. Nature. 2003;423: 173–177.
1195 doi:10.1038/nature01618

1196 19. Ezan J, Montcouquiol M. Revisiting planar cell polarity in the inner ear. Semin Cell Dev Biol. 2013;24:
1197 499–506. doi:10.1016/j.semcdb.2013.03.012

1198 20. Goodrich LV. The plane facts of PCP in the CNS. Neuron. 2008;60: 9–16.
1199 doi:10.1016/j.neuron.2008.09.003

1200 21. Tissir F, Goffinet AM. Shaping the nervous system: role of the core planar cell polarity genes. Nat
1201 Rev Neurosci. 2013;14: 525–535. doi:10.1038/nrn3525

1202 22. Sans N, Ezan J, Moreau MM, Montcouquiol M. Planar Cell Polarity Gene Mutations in Autism
1203 Spectrum Disorder, Intellectual Disabilities, and Related Deletion/Duplication Syndromes. Neuronal
1204 and Synaptic Dysfunction in Autism Spectrum Disorder and Intellectual Disability. Elsevier; 2016. pp.
1205 189–219. doi:10.1016/B978-0-12-800109-7.00013-3

1206 23. Hakanen J, Ruiz-Reig N, Tissir F. Linking Cell Polarity to Cortical Development and Malformations.
1207 Frontiers in Cellular Neuroscience. 2019;13. doi:10.3389/fncel.2019.00244

1208 24. Wada H, Iwasaki M, Sato T, Masai I, Nishiwaki Y, Tanaka H, et al. Dual roles of zygotic and maternal
1209 Scribble1 in neural migration and convergent extension movements in zebrafish embryos.
1210 Development. 2005;132: 2273–2285. doi:10.1242/dev.01810

1211 25. Walsh GS, Grant PK, Morgan JA, Moens CB. Planar polarity pathway and Nance-Horan syndrome-like
1212 1b have essential cell-autonomous functions in neuronal migration. Development. 2011;138: 3033–
1213 3042. doi:10.1242/dev.063842

1214 26. Jarjour AA, Boyd A, Dow LE, Holloway RK, Goebbels S, Humbert PO, et al. The polarity protein
1215 Scribble regulates myelination and remyelination in the central nervous system. PLoS Biol. 2015;13:
1216 e1002107. doi:10.1371/journal.pbio.1002107

1217 27. Moreau MM, Piguel N, Papouin T, Koehl M, Durand CM, Rubio ME, et al. The planar polarity protein
1218 Scribble1 is essential for neuronal plasticity and brain function. J Neurosci. 2010;30: 9738–9752.
1219 doi:10.1523/JNEUROSCI.6007-09.2010

1220 28. Piguel NH, Fievre S, Blanc J-M, Carta M, Moreau MM, Moutin E, et al. Scribble1/AP2 complex
1221 coordinates NMDA receptor endocytic recycling. Cell Rep. 2014;9: 712–727.
1222 doi:10.1016/j.celrep.2014.09.017

1223 29. Hilal ML, Moreau MM, Racca C, Pinheiro VL, Piguel NH, Santoni M-J, et al. Activity-Dependent
1224 Neuroplasticity Induced by an Enriched Environment Reverses Cognitive Deficits in Scribble
1225 Deficient Mouse. Cereb Cortex. 2017;27: 5635–5651. doi:10.1093/cercor/bhw333

1226 30. Robinson A, Escuin S, Doudney K, Vekemans M, Stevenson RE, Greene NDE, et al. Mutations in the
1227 planar cell polarity genes CELSR1 and SCRIB are associated with the severe neural tube defect
1228 craniorachischisis. Hum Mutat. 2012;33: 440–447. doi:10.1002/humu.21662

1229 31. Lei Y, Zhu H, Duhon C, Yang W, Ross ME, Shaw GM, et al. Mutations in planar cell polarity gene
1230 SCRIB are associated with spina bifida. PLoS ONE. 2013;8: e69262.
1231 doi:10.1371/journal.pone.0069262

1232 32. Kharfallah F, Guyot MC, El Hassan AR, Allache R, Merello E, De Marco P, et al. Scribble1 plays an
1233 important role in the pathogenesis of neural tube defects through its mediating effect of Par-3 and
1234 Vangl1/2 localization. Hum Mol Genet. 2017;26: 2307–2320. doi:10.1093/hmg/ddx122

1235 33. Gavériaux-Ruff C, Kieffer BL. Conditional gene targeting in the mouse nervous system: Insights into
1236 brain function and diseases. Pharmacol Ther. 2007;113: 619–634.
1237 doi:10.1016/j.pharmthera.2006.12.003

1238 34. Montcouquiol M, Sans N, Huss D, Kach J, Dickman JD, Forge A, et al. Asymmetric localization of
1239 Vangl2 and Fz3 indicate novel mechanisms for planar cell polarity in mammals. J Neurosci. 2006;26:
1240 5265–5275. doi:10.1523/JNEUROSCI.4680-05.2006

1241 35. Mendes SW, Henkemeyer M, Liebl DJ. Multiple Eph receptors and B-class ephrins regulate midline
1242 crossing of corpus callosum fibers in the developing mouse forebrain. J Neurosci. 2006;26: 882–892.
1243 doi:10.1523/JNEUROSCI.3162-05.2006

1244 36. Yamben IF, Rachel RA, Shatadal S, Copeland NG, Jenkins NA, Warming S, et al. Scrib is required for
1245 epithelial cell identity and prevents epithelial to mesenchymal transition in the mouse. Dev Biol.
1246 2013;384: 41–52. doi:10.1016/j.ydbio.2013.09.027

1247 37. Gorski JA, Talley T, Qiu M, Puelles L, Rubenstein JLR, Jones KR. Cortical excitatory neurons and glia,
1248 but not GABAergic neurons, are produced in the Emx1-expressing lineage. J Neurosci. 2002;22:
1249 6309–6314. doi:20026564

1250 38. Hébert JM, McConnell SK. Targeting of cre to the Foxg1 (BF-1) locus mediates loxP recombination in
1251 the telencephalon and other developing head structures. Dev Biol. 2000;222: 296–306.
1252 doi:10.1006/dbio.2000.9732

1253 39. Madisen L, Zwingman TA, Sunkin SM, Oh SW, Zariwala HA, Gu H, et al. A robust and high-throughput
1254 Cre reporting and characterization system for the whole mouse brain. Nat Neurosci. 2010;13: 133–
1255 140. doi:10.1038/nn.2467

1256 40. Alcamo EA, Chirivella L, Dautzenberg M, Dobreva G, Fariñas I, Grosschedl R, et al. Satb2 regulates
1257 callosal projection neuron identity in the developing cerebral cortex. Neuron. 2008;57: 364–377.
1258 doi:10.1016/j.neuron.2007.12.012

1259 41. Britanova O, de Juan Romero C, Cheung A, Kwan KY, Schwark M, Gyorgy A, et al. Satb2 is a
1260 postmitotic determinant for upper-layer neuron specification in the neocortex. Neuron. 2008;57:
1261 378–392. doi:10.1016/j.neuron.2007.12.028

1262 42. Lindwall C, Fothergill T, Richards LJ. Commissure formation in the mammalian forebrain. Curr Opin
1263 Neurobiol. 2007;17: 3–14. doi:10.1016/j.conb.2007.01.008

1264 43. Paul LK, Brown WS, Adolphs R, Tyszka JM, Richards LJ, Mukherjee P, et al. Agenesis of the corpus
1265 callosum: genetic, developmental and functional aspects of connectivity. Nat Rev Neurosci. 2007;8:
1266 287–299. doi:10.1038/nrn2107

1267 44. Silver J, Lorenz SE, Wahlsten D, Coughlin J. Axonal guidance during development of the great
1268 cerebral commissures: descriptive and experimental studies, in vivo, on the role of preformed glial
1269 pathways. J Comp Neurol. 1982;210: 10–29. doi:10.1002/cne.902100103

1270 45. Shu T, Richards LJ. Cortical axon guidance by the glial wedge during the development of the corpus
1271 callosum. J Neurosci. 2001;21: 2749–2758.

1272 46. Shu T, Puche AC, Richards LJ. Development of midline glial populations at the corticoseptal
1273 boundary. J Neurobiol. 2003;57: 81–94. doi:10.1002/neu.10252

1274 47. Pan C, Cai R, Quacquarelli FP, Ghasemigharagoz A, Lourbopoulos A, Matryba P, et al. Shrinkage-
1275 mediated imaging of entire organs and organisms using uDISCO. Nature Methods. 2016;13: 859–
1276 867. doi:10.1038/nmeth.3964

1277 48. Goebbels S, Bormuth I, Bode U, Hermanson O, Schwab MH, Nave K-A. Genetic targeting of principal
1278 neurons in neocortex and hippocampus of NEX-Cre mice. Genesis. 2006;44: 611–621.
1279 doi:10.1002/dvg.20256

1280 49. Belvindrah R, Hankel S, Walker J, Patton BL, Müller U. Beta1 integrins control the formation of cell
1281 chains in the adult rostral migratory stream. J Neurosci. 2007;27: 2704–2717.
1282 doi:10.1523/JNEUROSCI.2991-06.2007

1283 50. Rivero O, Selten MM, Sich S, Popp S, Bacmeister L, Amendola E, et al. Cadherin-13, a risk gene for
1284 ADHD and comorbid disorders, impacts GABAergic function in hippocampus and cognition. Transl
1285 Psychiatry. 2015;5: e655. doi:10.1038/tp.2015.152

1286 51. Pulvers JN, Bryk J, Fish JL, Wilsch-Bräuninger M, Arai Y, Schreier D, et al. Mutations in mouse Aspm
1287 (abnormal spindle-like microcephaly associated) cause not only microcephaly but also major defects
1288 in the germline. Proc Natl Acad Sci USA. 2010;107: 16595–16600. doi:10.1073/pnas.1010494107

1289 52. Evsyukova I, Plestant C, Anton ES. Integrative mechanisms of oriented neuronal migration in the
1290 developing brain. Annu Rev Cell Dev Biol. 2013;29: 299–353. doi:10.1146/annurev-cellbio-101512-
1291 122400

1292 53. Žigman M, Trinh LA, Fraser SE, Moens CB. Zebrafish neural tube morphogenesis requires Scribble-
1293 dependent oriented cell divisions. Curr Biol. 2011;21: 79–86. doi:10.1016/j.cub.2010.12.005

1294 54. Ono Y, Urata Y, Goto S, Nakagawa S, Humbert PO, Li T-S, et al. Muscle stem cell fate is controlled by
1295 the cell-polarity protein Scrib. Cell Rep. 2015;10: 1135–1148. doi:10.1016/j.celrep.2015.01.045

1296 55. Pham K, Shimoni R, Charnley M, Ludford-Menting MJ, Hawkins ED, Ramsbottom K, et al.
1297 Asymmetric cell division during T cell development controls downstream fate. J Cell Biol. 2015;210:
1298 933–950. doi:10.1083/jcb.201502053

1299 56. Briata P, Di Blas E, Gulisano M, Mallamaci A, Iannone R, Boncinelli E, et al. EMX1 homeoprotein is
1300 expressed in cell nuclei of the developing cerebral cortex and in the axons of the olfactory sensory
1301 neurons. Mech Dev. 1996;57: 169–180.

1302 57. Nakagawa Y, Johnson JE, O'Leary DD. Graded and areal expression patterns of regulatory genes and
1303 cadherins in embryonic neocortex independent of thalamocortical input. J Neurosci. 1999;19:
1304 10877–10885.

1305 58. Sun T, Yang L, Kaur H, Pestel J, Looso M, Nolte H, et al. A reverse signaling pathway downstream of
1306 Sema4A controls cell migration via Scrib. J Cell Biol. 2017;216: 199–215. doi:10.1083/jcb.201602002

1307 59. Vaughen J, Igaki T. Slit-Robo Repulsive Signaling Extrudes Tumorigenic Cells from Epithelia. Dev Cell.
1308 2016;39: 683–695. doi:10.1016/j.devcel.2016.11.015

1309 60. Gobius I, Morcom L, Suárez R, Bunt J, Bukshpun P, Reardon W, et al. Astroglial-Mediated
1310 Remodeling of the Interhemispheric Midline Is Required for the Formation of the Corpus Callosum.
1311 Cell Rep. 2016;17: 735–747. doi:10.1016/j.celrep.2016.09.033

1312 61. Yamaguchi Y, Miura M. How to form and close the brain: insight into the mechanism of cranial
1313 neural tube closure in mammals. Cell Mol Life Sci. 2013;70: 3171–3186. doi:10.1007/s00018-012-
1314 1227-7

1315 62. Yu H, Smallwood PM, Wang Y, Vidaltamayo R, Reed R, Nathans J. Frizzled 1 and frizzled 2 genes
1316 function in palate, ventricular septum and neural tube closure: general implications for tissue fusion
1317 processes. Development. 2010;137: 3707–3717. doi:10.1242/dev.052001

1318 63. Rachel RA, Murdoch JN, Beermann F, Copp AJ, Mason CA. Retinal axon misrouting at the optic
1319 chiasm in mice with neural tube closure defects. Genesis. 2000;27: 32–47.

1320 64. Sun SD, Purdy AM, Walsh GS. Planar cell polarity genes Frizzled3a, Vangl2, and Scribble are required
1321 for spinal commissural axon guidance. BMC Neurosci. 2016;17: 83. doi:10.1186/s12868-016-0318-z

1322 65. Edwards TJ, Sherr EH, Barkovich AJ, Richards LJ. Clinical, genetic and imaging findings identify new
1323 causes for corpus callosum development syndromes. Brain. 2014;137: 1579–1613.
1324 doi:10.1093/brain/awt358

1325 66. Mahmood S, Ahmad W, Hassan MJ. Autosomal Recessive Primary Microcephaly (MCPH): clinical
1326 manifestations, genetic heterogeneity and mutation continuum. Orphanet J Rare Dis. 2011;6: 39.
1327 doi:10.1186/1750-1172-6-39

1328 67. Nahorski MS, Asai M, Wakeling E, Parker A, Asai N, Canham N, et al. CCDC88A mutations cause
1329 PEHO-like syndrome in humans and mouse. Brain. 2016;139: 1036–1044.
1330 doi:10.1093/brain/aww014

1331 68. Doherty D, Chudley AE, Coghlan G, Ishak GE, Innes AM, Lemire EG, et al. GPSM2 mutations cause
1332 the brain malformations and hearing loss in Chudley-McCullough syndrome. Am J Hum Genet.
1333 2012;90: 1088–1093. doi:10.1016/j.ajhg.2012.04.008

1334 69. Mauriac SA, Hien YE, Bird JE, Carvalho SD-S, Peyroutou R, Lee SC, et al. Defective Gpsm2/Gαi3
1335 signalling disrupts stereocilia development and growth cone actin dynamics in Chudley-McCullough
1336 syndrome. Nat Commun. 2017;8: 14907. doi:10.1038/ncomms14907

1337 70. Richards LJ, Plachez C, Ren T. Mechanisms regulating the development of the corpus callosum and
1338 its agenesis in mouse and human. Clin Genet. 2004;66: 276–289. doi:10.1111/j.1399-
1339 0004.2004.00354.x

1340 71. Cervantes-Sandoval I, Chakraborty M, MacMullen C, Davis RL. Scribble Scaffolds a Signalosome for
1341 Active Forgetting. Neuron. 2016;90: 1230–1242. doi:10.1016/j.neuron.2016.05.010

1342 72. Stergiakouli E, Davey Smith G, Martin J, Skuse DH, Viechtbauer W, Ring SM, et al. Shared genetic
1343 influences between dimensional ASD and ADHD symptoms during child and adolescent
1344 development. Mol Autism. 2017;8: 18. doi:10.1186/s13229-017-0131-2

1345 73. Naaijen J, Bralten J, Poelmans G, IMAGE consortium, Glennon JC, Franke B, et al. Glutamatergic and
1346 GABAergic gene sets in attention-deficit/hyperactivity disorder: association to overlapping traits in
1347 ADHD and autism. Transl Psychiatry. 2017;7: e999. doi:10.1038/tp.2016.273

1348 74. Phillips HM, Rhee HJ, Murdoch JN, Hildreth V, Peat JD, Anderson RH, et al. Disruption of planar cell
1349 polarity signaling results in congenital heart defects and cardiomyopathy attributable to early
1350 cardiomyocyte disorganization. Circ Res. 2007;101: 137–145. doi:10.1161/CIRCRESAHA.106.142406

1351 75. Boczonadi V, Gillespie R, Keenan I, Ramsbottom SA, Donald-Wilson C, Al Nazer M, et al. Scrib:Rac1
1352 interactions are required for the morphogenesis of the ventricular myocardium. Cardiovasc Res.
1353 2014;104: 103–115. doi:10.1093/cvr/cvu193

1354 76. Wells C, Spaggiari E, Malan V, Stirnemann JJ, Attie-Bitach T, Ville Y, et al. First fetal case of the
1355 8q24.3 contiguous genes syndrome. Am J Med Genet A. 2016;170A: 239–242.
1356 doi:10.1002/ajmg.a.37411

1357 77. Hocking JC, Famulski JK, Yoon KH, Widen SA, Bernstein CS, Koch S, et al. Morphogenetic defects
1358 underlie Superior Coloboma, a newly identified closure disorder of the dorsal eye. PLoS Genet.
1359 2018;14: e1007246. doi:10.1371/journal.pgen.1007246

1360 78. Skouloudaki K, Puetz M, Simons M, Courbard J-R, Boehlke C, Hartleben B, et al. Scribble participates
1361 in Hippo signaling and is required for normal zebrafish pronephros development. Proc Natl Acad Sci
1362 USA. 2009;106: 8579–8584. doi:10.1073/pnas.0811691106

1363 79. Hartleben B, Widmeier E, Wanner N, Schmidts M, Kim ST, Schneider L, et al. Role of the polarity
1364 protein Scribble for podocyte differentiation and maintenance. PLoS ONE. 2012;7: e36705.
1365 doi:10.1371/journal.pone.0036705

1366 80. Murdoch JN, Henderson DJ, Doudney K, Gaston-Massuet C, Phillips HM, Paternotte C, et al.
1367 Disruption of scribble (Scrb1) causes severe neural tube defects in the circletail mouse. Hum Mol
1368 Genet. 2003;12: 87–98.

1369 81. Ezan J, Lasvaux L, Gezer A, Novakovic A, May-Simera H, Belotti E, et al. Primary cilium migration
1370 depends on G-protein signalling control of subapical cytoskeleton. Nature Cell Biology. 2013;15:
1371 1107–1115. doi:10.1038/ncb2819

1372 82. Guo H, Hong S, Jin X-L, Chen R-S, Avasthi PP, Tu Y-T, et al. Specificity and Efficiency of Cre-Mediated
1373 Recombination in Emx1–cre Knock-in Mice. Biochemical and Biophysical Research Communications.
1374 2000;273: 661–665. doi:10.1006/bbrc.2000.2870

1375 83. Bush JO, Soriano P. Ephrin-B1 regulates axon guidance by reverse signaling through a PDZ-
1376 dependent mechanism. Genes & Development. 2009;23: 1586–1599. doi:10.1101/gad.1807209

1377 84. Zhou L, Bar I, Achouri Y, Campbell K, De Backer O, Hebert JM, et al. Early Forebrain Wiring: Genetic
1378 Dissection Using Conditional Celsr3 Mutant Mice. Science. 2008;320: 946–949.
1379 doi:10.1126/science.1155244

1380 85. Giese AP, Ezan J, Wang L, Lasvaux L, Lembo F, Mazzocco C, et al. Gipc1 has a dual role in Vangl2
1381 trafficking and hair bundle integrity in the inner ear. Development. 2012;139: 3775–3785.
1382 doi:10.1242/dev.074229

1383 86. Kalinovsky A, Boukhtouche F, Blazeski R, Bornmann C, Suzuki N, Mason CA, et al. Development of
1384 Axon-Target Specificity of Ponto-Cerebellar Afferents. Polleux F, editor. PLoS Biology. 2011;9:
1385 e1001013. doi:10.1371/journal.pbio.1001013

1386 87. Calderon de Anda F, Rosario AL, Durak O, Tran T, Gräff J, Meletis K, et al. Autism spectrum disorder
1387 susceptibility gene TAOK2 affects basal dendrite formation in the neocortex. Nature Neuroscience.
1388 2012;15: 1022–1031. doi:10.1038/nn.3141

1389 88. Weissgerber TL, Milic NM, Winham SJ, Garovic VD. Beyond Bar and Line Graphs: Time for a New
1390 Data Presentation Paradigm. PLOS Biology. 2015;13: e1002128. doi:10.1371/journal.pbio.1002128

1391

1392

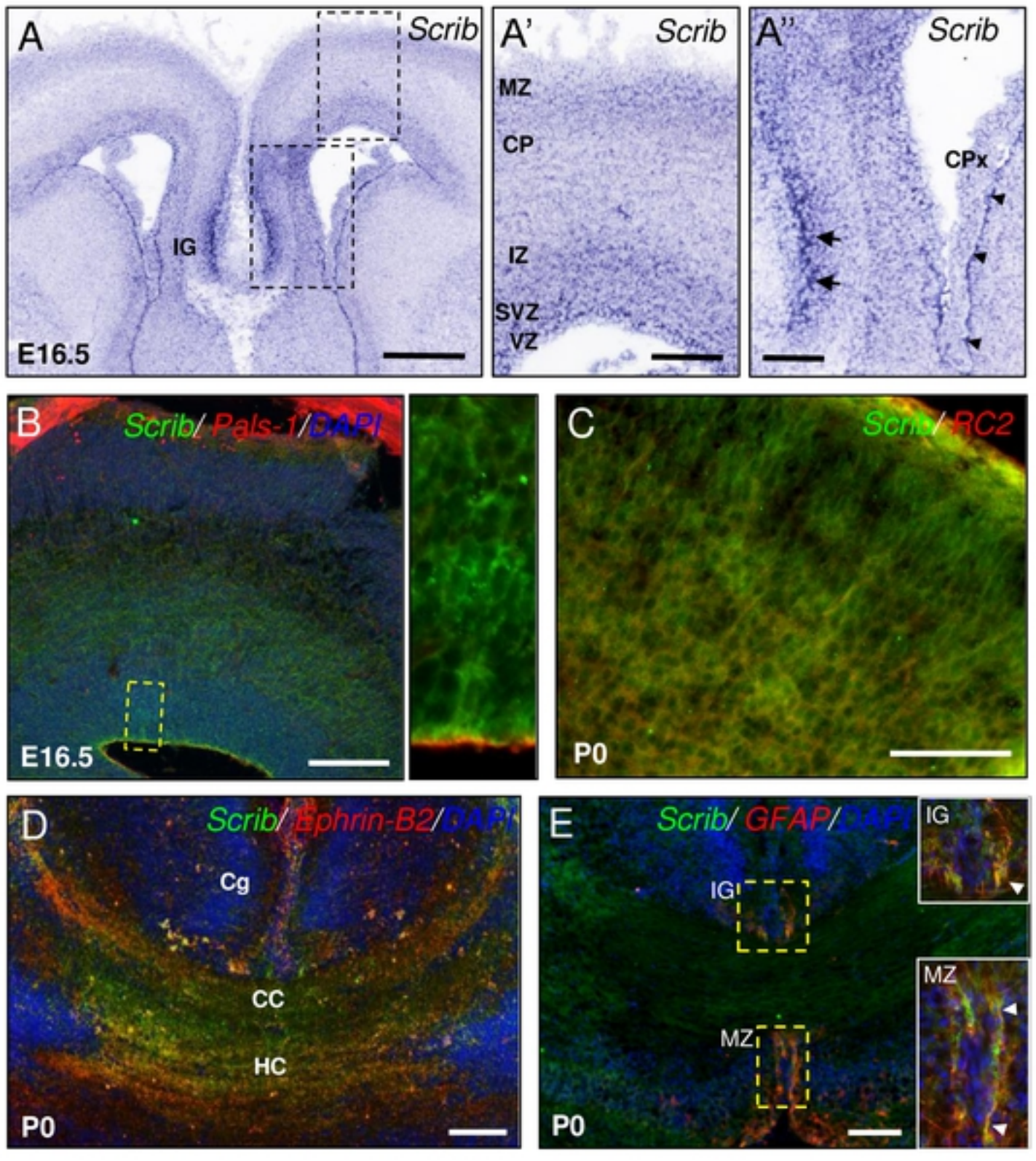
A
Scrib
IG
E16.5
A'
Scrib
MZ
CP
IZ
SVZ
VZ
A''
Scrib
CPx
B
Scrib/ Pals-1/DAPI
E16.5
C
Scrib/ RC2
P0
D
Scrib/ Ephrin-B2/DAPI
Cg
CC
HC
P0
E
Scrib/ GFAP/DAPI
IG
MZ
P0

Figure 1

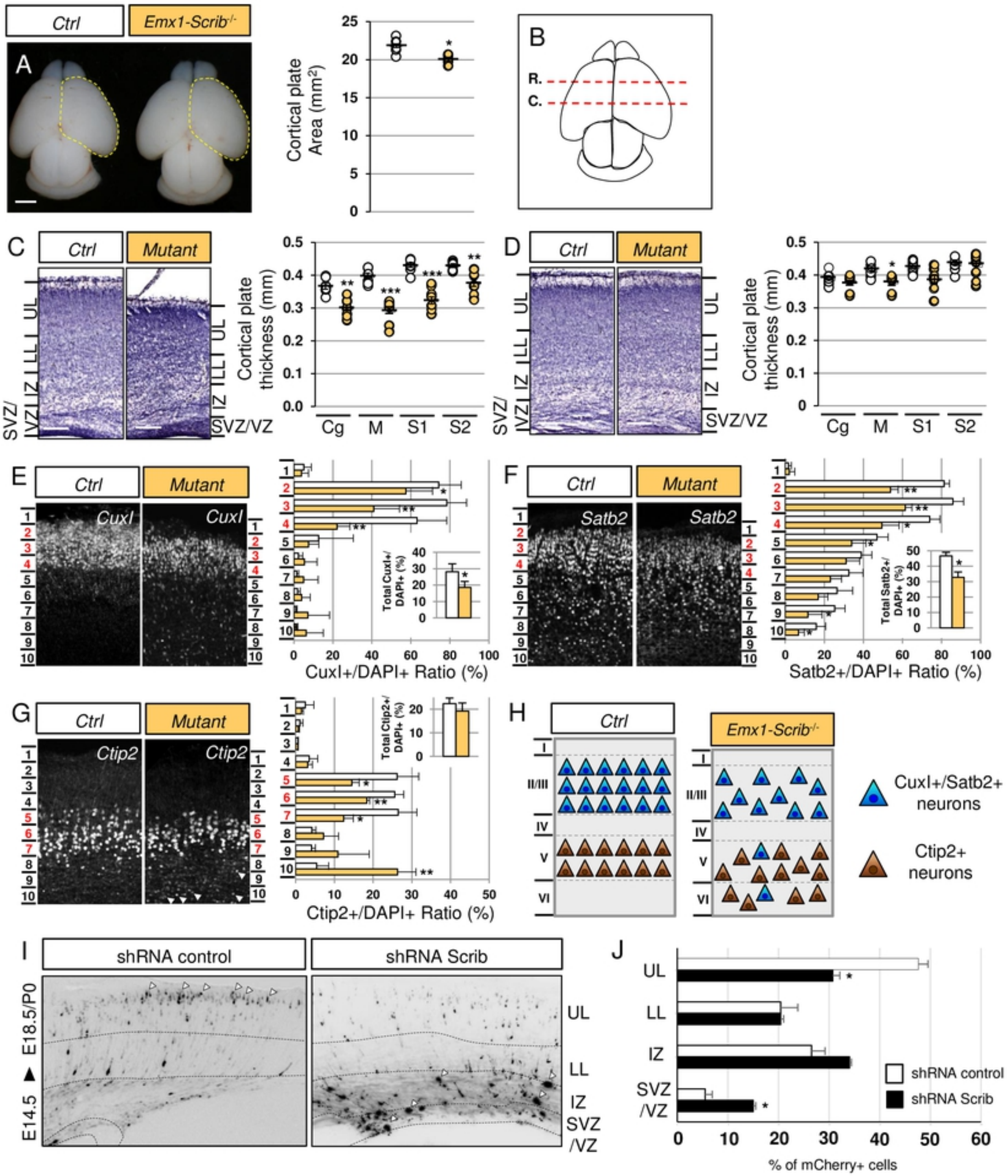
Ctrl
Emx1-Scrib-/-
A
Cortical plate Area (mm2)
B
R.
C.
C
Ctrl
Mutant
UL
LL
IZ
SVZ/VZ
Cortical plate thickness (mm)
Cg
M
S1
S2
D
E
CuxI
CuxI+/DAPI+ Ratio (%)
Total CuxI+/DAPI+ (%)
F
Satb2
Satb2+/DAPI+ Ratio (%)
Total Satb2+/DAPI+ (%)
G
Ctip2
Ctip2+/DAPI+ Ratio (%)
Total Ctip2+/DAPI+ (%)
H
I
II/III
IV
V
VI
CuxI+/Satb2+ neurons
Ctip2+ neurons
shRNA control
shRNA Scrib
E14.5 ▶ E18.5/P0
J
% of mCherry+ cells

Figure 2

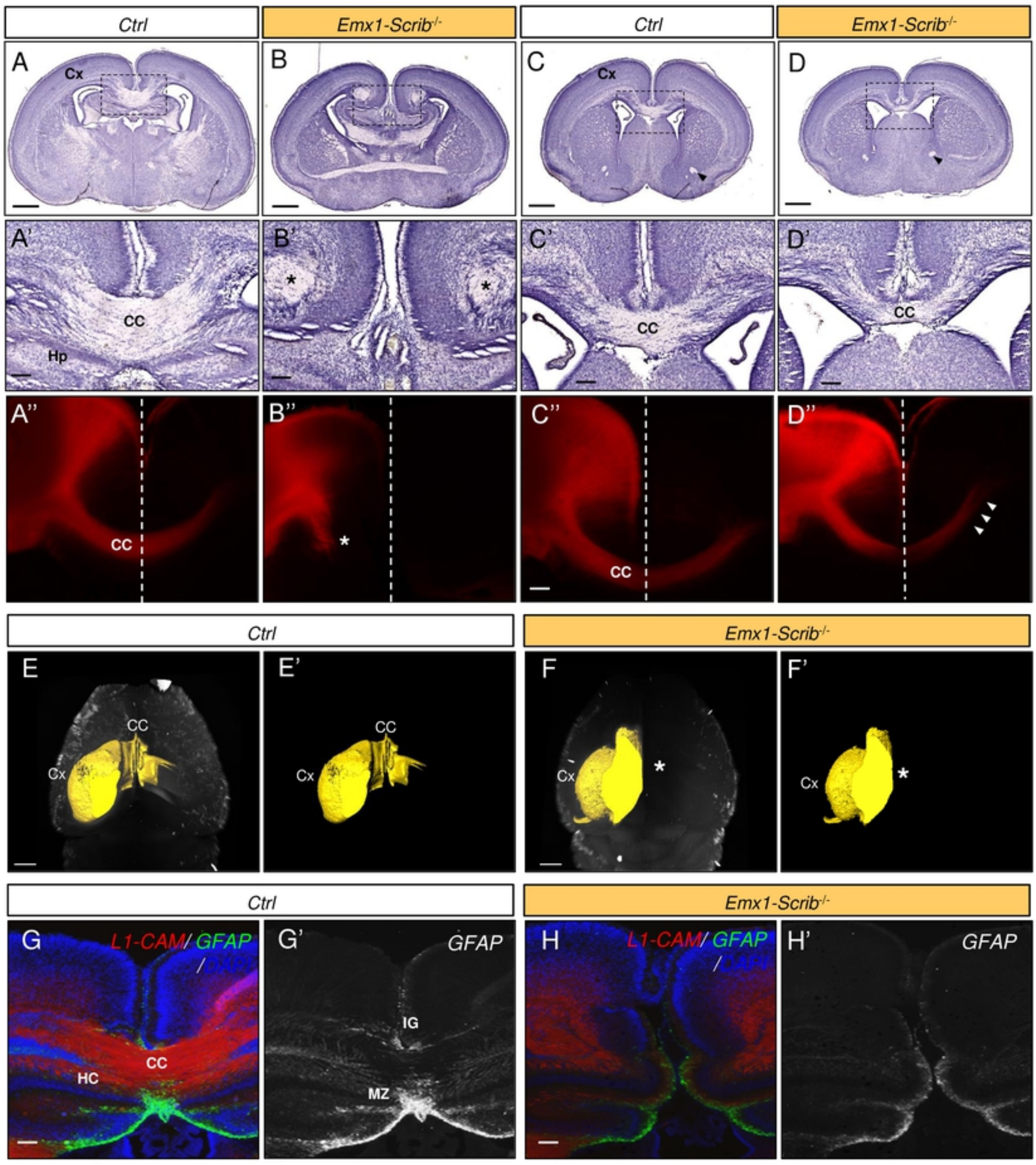
Ctrl
Emx1-Scrib-/-
Ctrl
Emx1-Scrib-/-
A
Cx
B
C
Cx
D
A'
CC
Hp
B'
*
*
C'
CC
D'
CC
A''
CC
B''
*
C''
CC
D''
Ctrl
Emx1-Scrib-/-
E
CC
Cx
E'
CC
Cx
F
Cx
*
F'
Cx
*
Ctrl
Emx1-Scrib-/-
G
L1-CAM/ GFAP
/ DAPI
CC
HC
G'
GFAP
IG
MZ
H
L1-CAM/ GFAP
/ DAPI
H'
GFAP

Figure 3

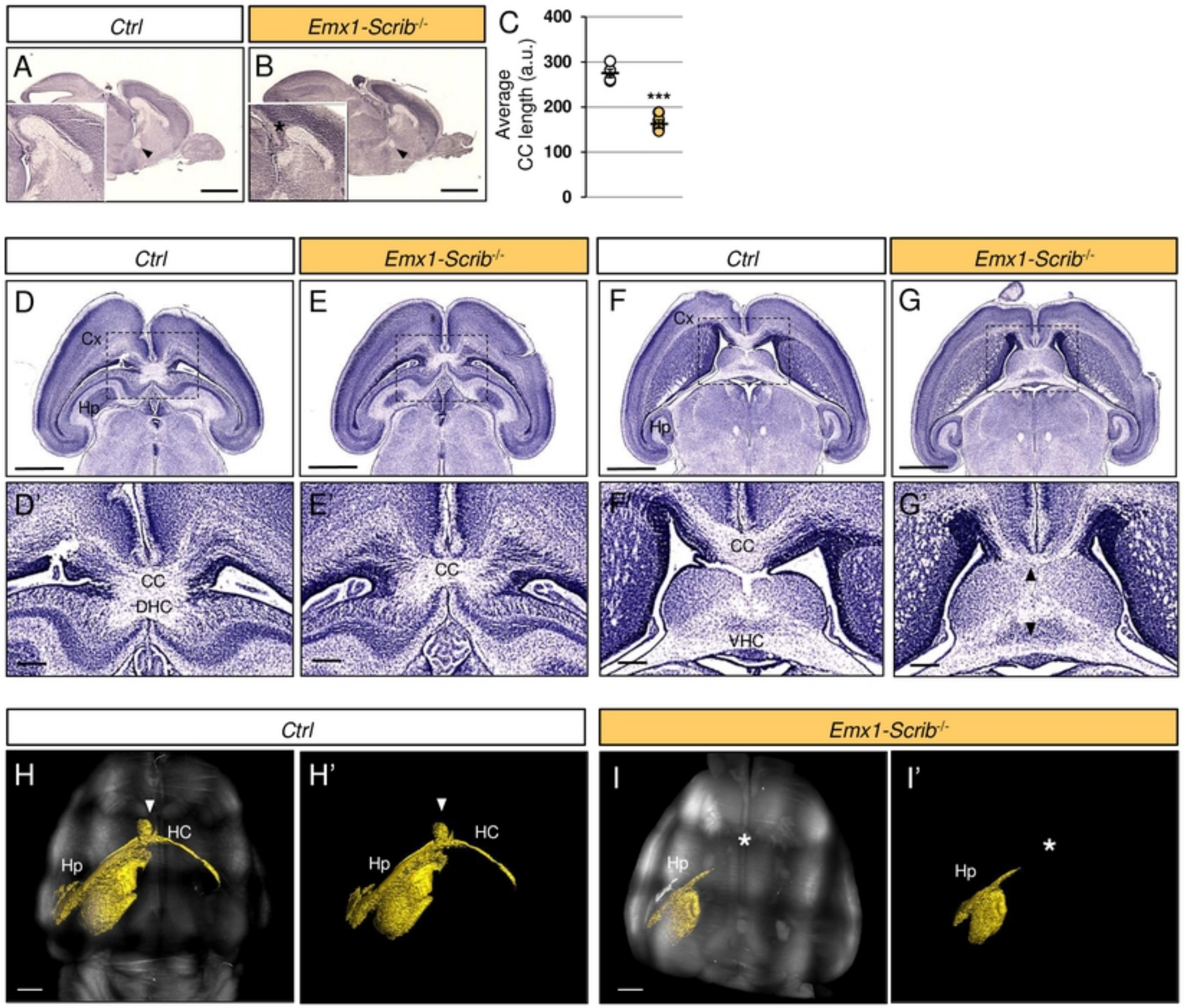
Ctrl
Emx1-Scrib-/-
A
B
C
Average CC length (a.u.)
400
300
200
100
0
***
D
E
F
G
Cx
Hp
D'
E'
F'
G'
CC
DHC
VHC
H
H'
I
I'
HC
*

Figure 4

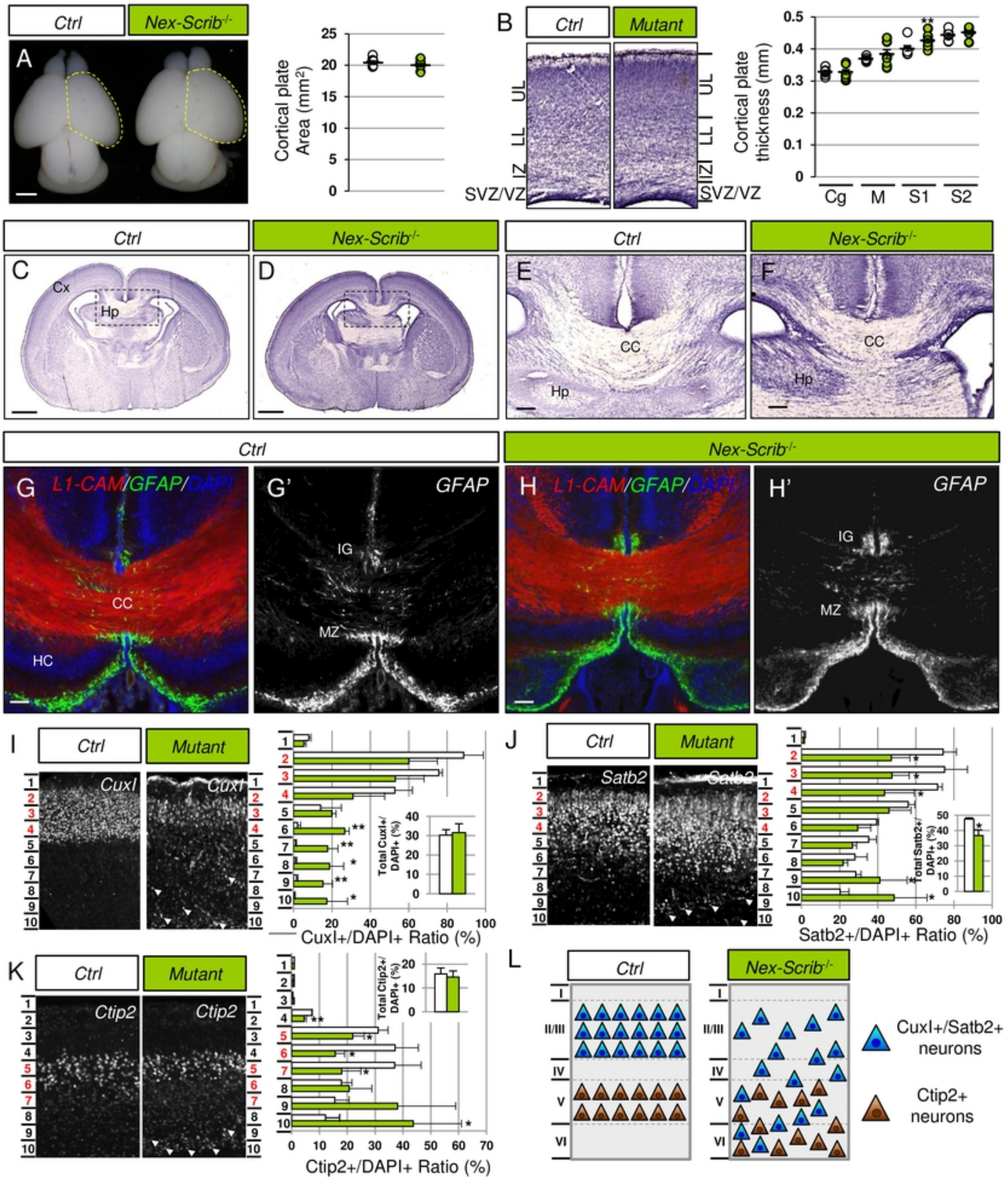
Ctrl
Nex-Scrib-/-
A
Cortical plate Area (mm2)
B
Mutant
UL
LL
IZ
SVZ/VZ
Cortical plate thickness (mm)
Cg
M
S1
S2
C
D
E
F
Cx
Hp
CC
G
L1-CAM/GFAP/DAPI
G'
GFAP
IG
MZ
HC
H
H'
I
J
K
L
Cuxl
Satb2
Ctip2
Total Cuxl+/DAPI+ (%)
Total Satb2+/DAPI+ (%)
Total Ctip2+/DAPI+ (%)
Cuxl+/DAPI+ Ratio (%)
Satb2+/DAPI+ Ratio (%)
Ctip2+/DAPI+ Ratio (%)
I
II/III
IV
V
VI
Cuxl+/Satb2+ neurons
Ctip2+ neurons

Figure 5

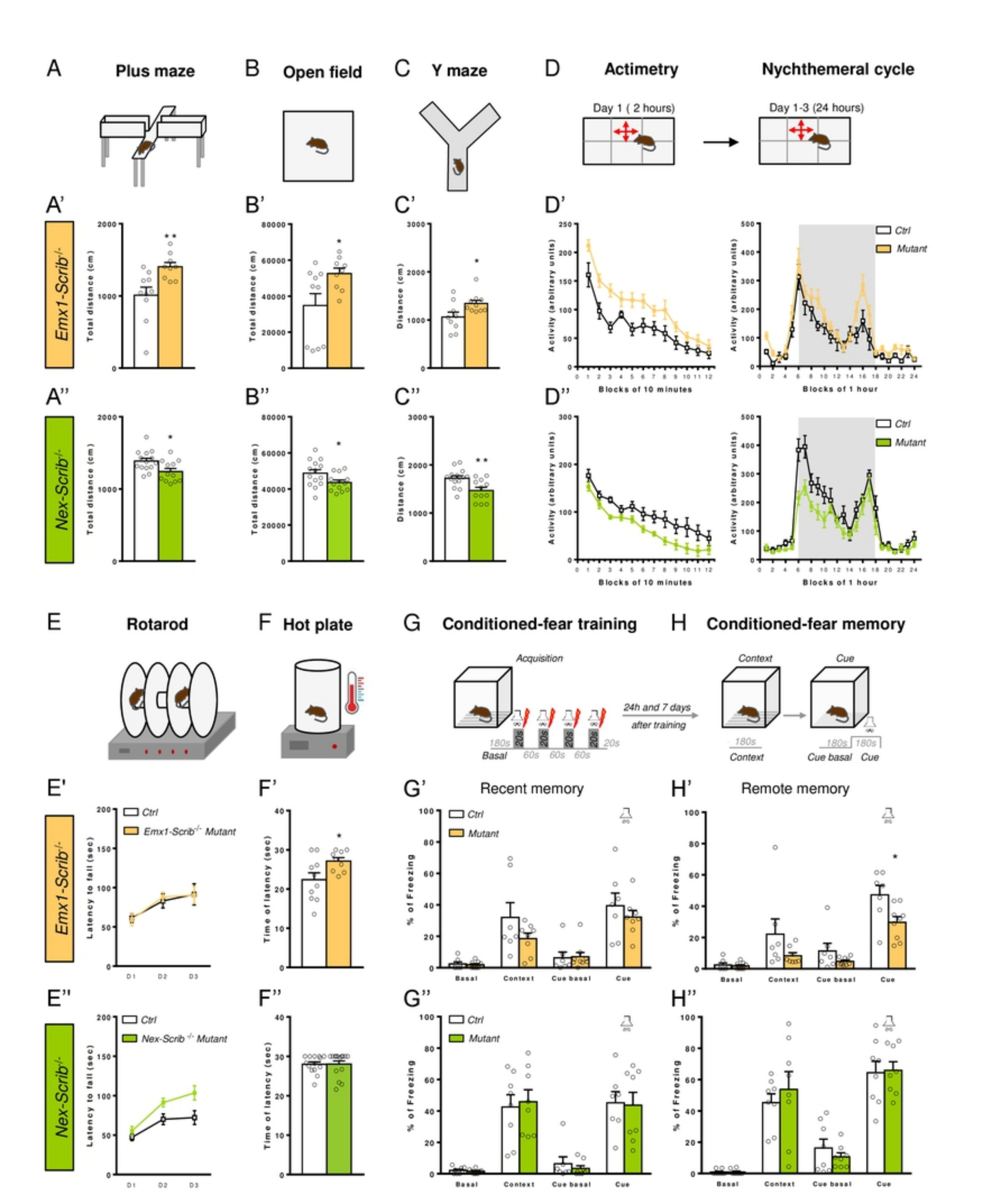
A
Plus maze
B
Open field
C
Y maze
D
Actimetry
Nychthemeral cycle
Day 1 (2 hours)
Day 1-3 (24 hours)
A'
B'
C'
D'
Emx1-Scrib-/-
Total distance (cm)
Distance (cm)
Activity (arbitrary units)
Blocks of 10 minutes
Blocks of 1 hour
Ctrl
Mutant
A''
B''
C''
D''
Nex-Scrib-/-
E
Rotarod
F
Hot plate
G
Conditioned-fear training
H
Conditioned-fear memory
Acquisition
24h and 7 days
after training
Basal
Context
Cue basal
Cue
E'
F'
G'
Recent memory
H'
Remote memory
Latency to fall (sec)
Time of latency (sec)
% of Freezing
Emx1-Scrib-/- Mutant
E''
F''
G''
H''
Nex-Scrib -/- Mutant

Figure 6

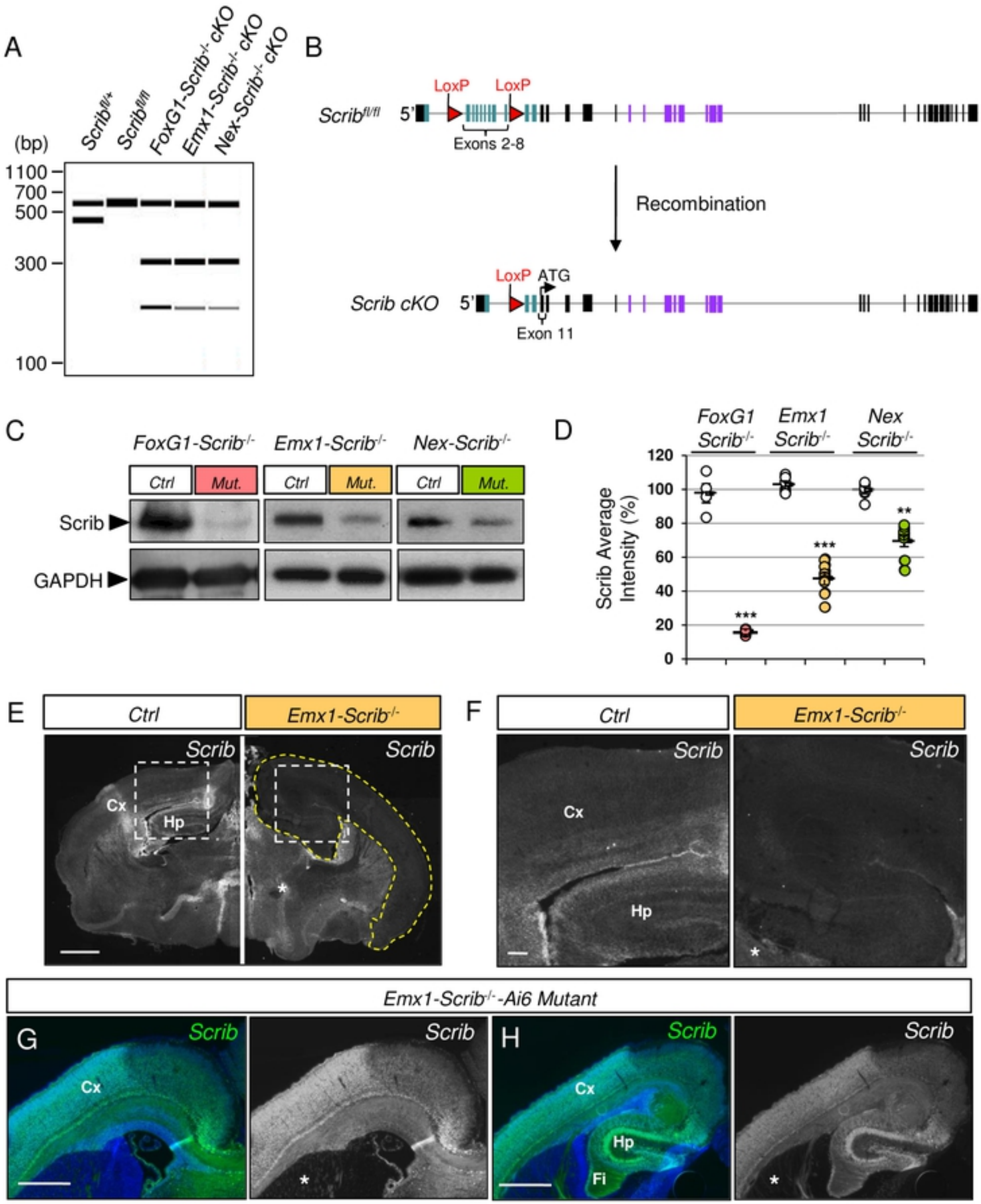
A
Scrib fl/+
Scrib fl/fl
FoxG1-Scrib-/- cKO
Emx1-Scrib-/- cKO
Nex-Scrib-/- cKO
(bp)
1100
700
500
300
100
B
Scrib fl/fl
5'
LoxP
LoxP
Exons 2-8
3'
Recombination
Scrib cKO
LoxP
ATG
Exon 11
C
FoxG1-Scrib-/-
Emx1-Scrib-/-
Nex-Scrib-/-
Ctrl
Mut.
Scrib
GAPDH
D
FoxG1 Scrib-/-
Emx1 Scrib-/-
Nex Scrib-/-
Scrib Average Intensity (%)
120
100
80
60
40
20
0
***
***
**
E
Ctrl
Emx1-Scrib-/-
Scrib
Cx
Hp
F
Ctrl
Emx1-Scrib-/-
Scrib
Cx
Hp
Emx1-Scrib-/--Ai6 Mutant
G
Scrib
Cx
H
Scrib
Cx
Hp
Fi

Figure S1

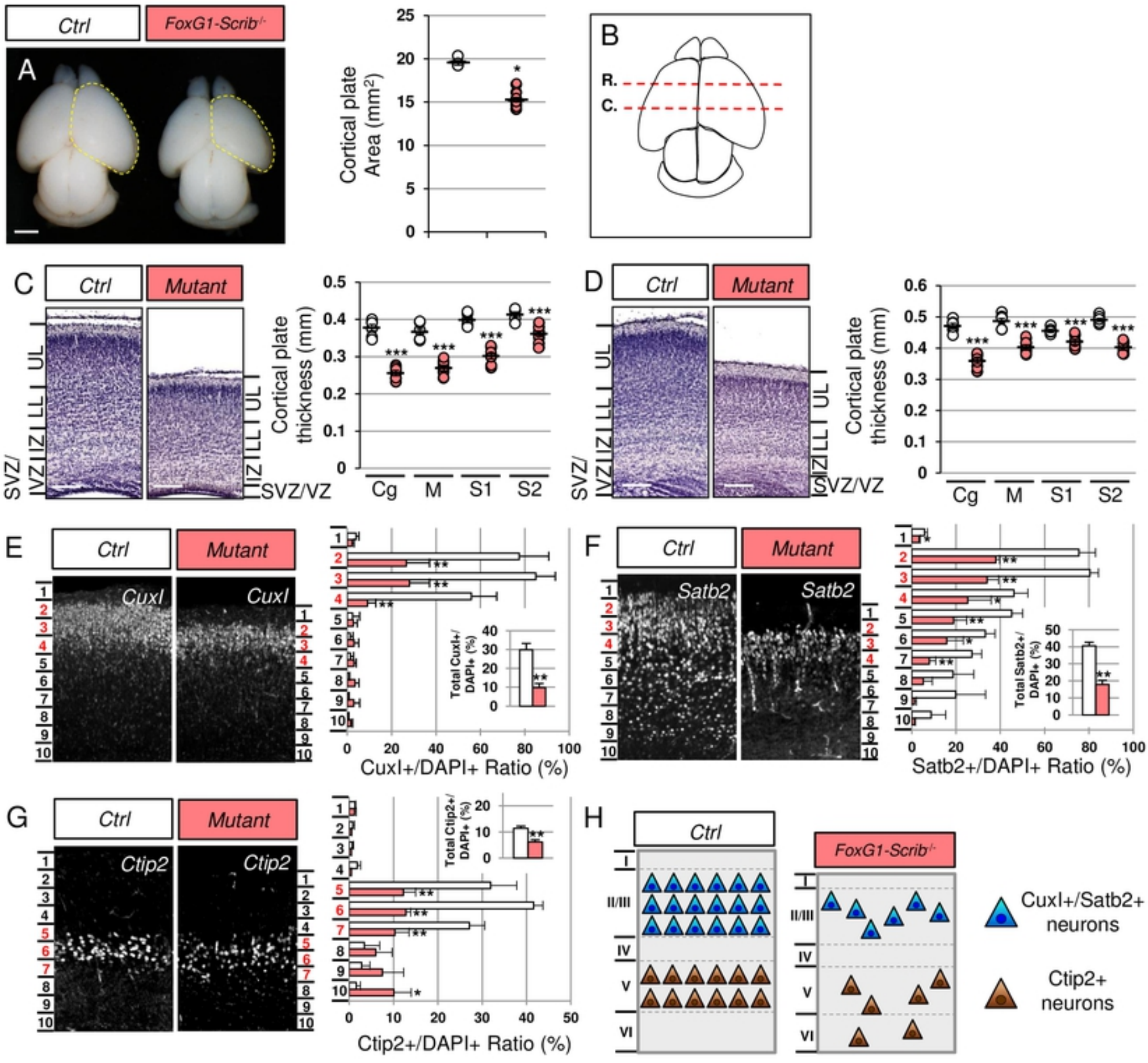
Ctrl
FoxG1-Scrib-/-
A
Cortical plate Area (mm2)
B
R.
C.
C
Ctrl
Mutant
SVZ/VZ
IZ
LL
UL
Cortical plate thickness (mm)
Cg
M
S1
S2
D
E
CuxI
CuxI+/DAPI+ Ratio (%)
Total CuxI+/DAPI+ (%)
F
Satb2
Satb2+/DAPI+ Ratio (%)
Total Satb2+/DAPI+ (%)
G
Ctip2
Ctip2+/DAPI+ Ratio (%)
Total Ctip2+/DAPI+ (%)
H
I
II/III
IV
V
VI
CuxI+/Satb2+ neurons
Ctip2+ neurons

Figure S2

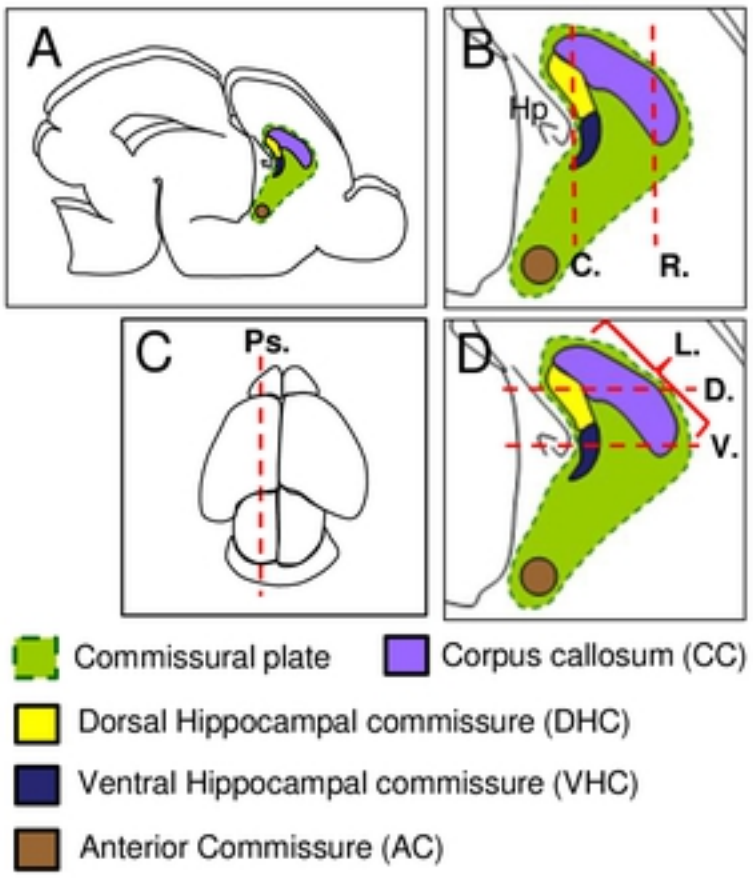
A
B
Hp
C.
R.
C
Ps.
D
L.
D.
V.
Commissural plate
Corpus callosum (CC)
Dorsal Hippocampal commissure (DHC)
Ventral Hippocampal commissure (VHC)
Anterior Commissure (AC)

Figure S3

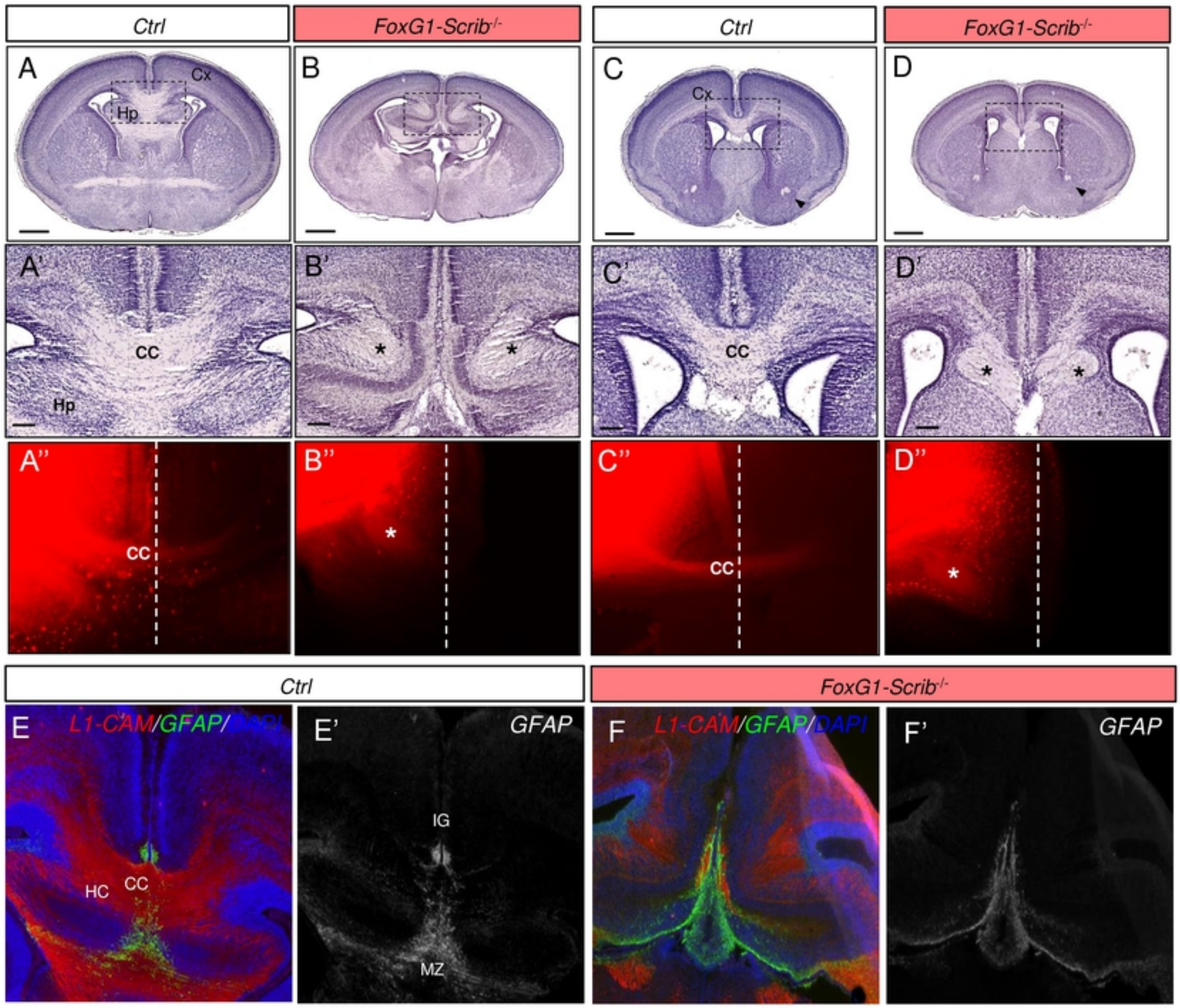
Ctrl
FoxG1-Scrib-/-
Ctrl
FoxG1-Scrib-/-
A
Cx
Hp
B
C
Cx
D
A'
CC
Hp
B'
*
*
C'
CC
D'
*
*
A''
CC
B''
*
C''
CC
D''
*
Ctrl
FoxG1-Scrib-/-
E
L1-CAM/GFAP/DAPI
HC
CC
E'
GFAP
IG
MZ
F
L1-CAM/GFAP/DAPI
F'
GFAP

Figure S4

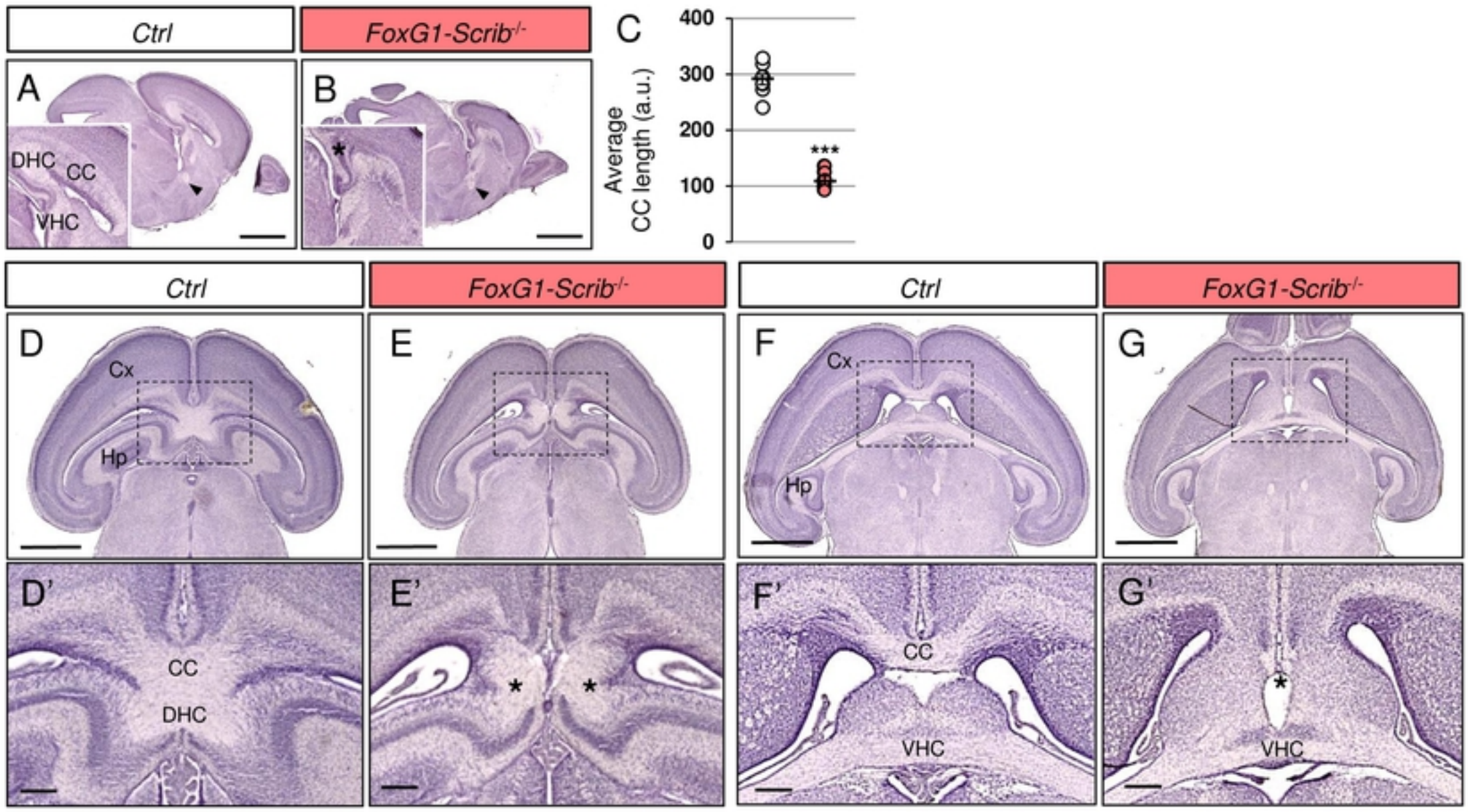
Ctrl
FoxG1-Scrib-/-
A
B
C
DHC
CC
VHC
*
Average CC length (a.u.)
400
300
200
100
0
***
D
E
F
G
Cx
Hp
D'
E'
F'
G'
CC
DHC
VHC

Figure S5

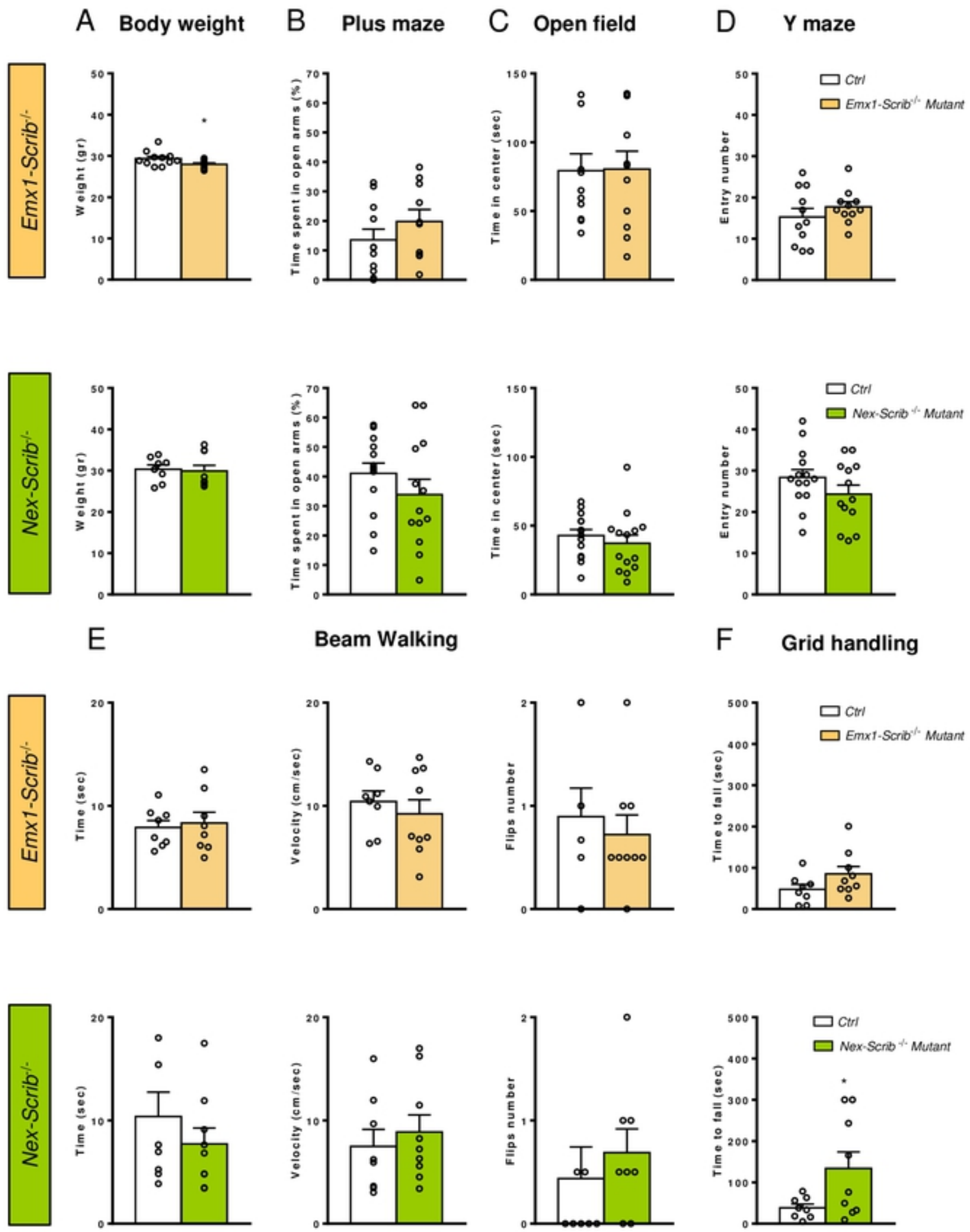
A Body weight
B Plus maze
C Open field
D Y maze
Emx1-Scrib-/-
Nex-Scrib-/-
Weight (gr)
Time spent in open arms (%)
Time in center (sec)
Entry number
Ctrl
Emx1-Scrib-/- Mutant
Nex-Scrib -/- Mutant
E Beam Walking
F Grid handling
Time (sec)
Velocity (cm/sec)
Flips number
Time to fall (sec)

Figure S6